Trial Version



Demographics of Triple Systems in Dense Star Clusters

Giacomo Fragione^{1,2}, Miguel A. S. Martinez^{1,2}, Kyle Kremer^{1,2}, Sourav Chatterjee³, Carl L. Rodriguez⁴, Claire S. Ye^{1,2}, Newlin C. Weatherford^{1,2}, Smadar Naoz^{5,6}, and Frederic A. Rasio^{1,2} Department of Physics & Astronomy, Northwestern University, Evanston, IL 60208, USA; giacomo.fragione@northwestern.edu ² Center for Interdisciplinary Exploration & Research in Astrophysics (CIERA), Northwestern University, Evanston, IL 60208, USA Department of Astronomy & Astrophysics, Tata Institute of Fundamental Research, Homi Bhabha Road, Navy Nagar, Colaba, Mumbai 400005, India Astronomy Department, Harvard University, 60 Garden St., Cambridge, MA 02138, USA ⁵ Department of Physics and Astronomy, University of California, Los Angeles, CA 90095, USA ⁶ Mani L. Bhaumik Institute for Theoretical Physics, UCLA, Los Angeles, CA 90095, USA Received 2020 July 3; revised 2020 July 21; accepted 2020 July 21; published 2020 August 27

Abstract

Depending on the stellar type, more than 15% of stars in the field have at least two stellar companions. Hierarchical triple systems can be assembled dynamically in dense star clusters, as a result of few-body encounters among stars and/or compact remnants in the cluster core. In this paper, we present the demographics of stellar and compactobject triples formed via binary-binary encounters in the CMC Cluster Catalog, a suite of cluster simulations with present-day properties representative of the globular clusters (GCs) observed in the Milky Way. We show how the initial properties of the host cluster set the typical orbital parameters and formation times of the formed triples. We find that a cluster typically assembles hundreds of triples with at least one black hole (BH) in the inner binary, while only clusters with sufficiently small virial radii are efficient in producing triples with no BHs. We show that a typical GC is expected to host tens of triples with at least one luminous component at present. We discuss how the Lidov-Kozai mechanism can drive the inner binary of these dynamically formed triples to high eccentricities, whenever it takes place before the triple is dynamically reprocessed by encountering another cluster member. Some of these systems can reach sufficiently large eccentricities to form a variety of transients and merger products, such as blue stragglers, X-ray binaries, Type Ia supernovae, Thorne-Zytkow objects, and gravitational wave sources.

Unified Astronomy Thesaurus concepts: Astrophysical black holes (98); Gravitational waves (678); Stellar mass black holes (1611); Globular star clusters (656); Star clusters (1567); Trinary stars (1714); Neutron stars (1108); Gravitational wave astronomy (675); Galaxy clusters (584); Milky Way Galaxy (1054); Milky Way dynamics (1051); Blue straggler stars (168)

1. Introduction

Stellar multiplicity is an omnipresent outcome of the star formation process (Duchêne & Kraus 2013). More than \sim 50% of stars are thought to have at least one stellar companion (e.g., Tokovinin 2014). Stephan et al. (2014) showed that at least \sim 13% of F-type and G-type dwarf stars in the Hipparcos sample live in triple systems (an inner binary orbited by an outer companion), while Riddle et al. (2015) found a relatively large abundance of 2 + 2 quadruples (a binary where the components are themselves binaries) with Robo-AO, the first robotic adaptive optics instrument. Sana et al. (2014) estimated that \sim 80% of O-type stars have at least one companion and $\sim 25\%$ have at least two such companions in their sample. Using a large high-resolution radial velocity spectroscopic survey of B-type and O-type stars, Chini et al. (2012) estimated that at least 50%–80% of them are multiples. Recently, a black hole (BH) of $\sim 5 M$ has been claimed to live in the triple system HR 6819, \sim 300 pc from the Sun (Rivinius et al. 2020).

In dense star clusters, hierarchical systems of stars and/or compact remnants can form through few-body (particularly binary-binary) encounters in the clusters' dense cores (e.g., Fregeau et al. 2004; Leigh & Geller 2013; Antognini & Thompson 2016; Fragione et al. 2019d). In this process, one of the two binaries captures a component of the second binary, with the remaining object leaving the system. Leigh et al. (2016) estimated that the branching ratio of this process can be as high as \sim 10%, assuming all equal masses. Therefore, the following

questions arise naturally: What is the role of dense star clusters, such as globular clusters (GCs), in dynamically assembling triple systems? What are the properties of these triples? How does this process depend on cluster properties, such as mass, concentration, and metallicity?

GCs represent the ideal environment to study the importance of gravitational dynamics in dense stellar systems and how dynamics shape both cluster evolution and survival (see, e.g., Heggie & Hut 2003). Importantly, frequent dynamical encounters between cluster members are fundamental in creating and explaining the existence of a number of exotic populations, such as X-ray binaries (e.g., Clark 1975; Verbunt et al. 1984; Heinke et al. 2005; Ivanova 2013; Giesler et al. 2018; Kremer et al. 2018), radio sources (e.g., Lyne et al. 1987; Sigurdsson & Phinney 1995; Ivanova et al. 2008; Ransom 2008; Fragione et al. 2018; Ye et al. 2019), and gravitational wave (GW) binaries (e.g., Moody & Sigurdsson 2009; Banerjee et al. 2010; Rodriguez et al. 2015, 2016, 2018a; Askar et al. 2017; Banerjee 2017; Chatterjee et al. 2017a, 2017b; Fragione & Kocsis 2018; Hong et al. 2018; Samsing & D'Orazio 2018; Zevin et al. 2018; Kremer et al. 2019d). However, with the possible exception of Antonini et al. (2016), there have been no comprehensive studies about the origin of hierarchical systems in dense star clusters and how this depends on clusters' primordial properties.

What makes hierarchical triple and multiple systems of particular interest is that they can produce exotic objects, transients, and GW sources over a larger portion of the parameter space compared to binaries. This additional portion is enabled by

the Lidov-Kozai (LK) mechanism (Kozai 1962; Lidov 1962). In recent years, a number of authors have shown how hierarchical triples are efficient in producing GW sources (e.g., Petrovich & Antonini 2017; Hamers et al. 2018; Hoang et al. 2018; Fragione & Kocsis 2019, 2020; Liu et al. 2019; Stephan et al. 2019), tidal disruption events (e.g., Chen et al. 2009; Fragione & Leigh 2018; Fragione et al. 2019c), white dwarf (WD) mergers (e.g., Toonen et al. 2018; Fragione et al. 2019e), and millisecond pulsars (e.g., Ford et al. 2000). In this framework, the eccentricity of the inner binary is not constant, but rather oscillates between a minimum and a maximum value (determined by the triple initial configuration), due to the tidal force imposed by the third companion (for a review see Naoz 2016). As a result, the inner binary components may be efficiently driven to sufficiently small separations to merge either through physical collisions or dissipation by GW emission.

In this paper, we study the role of dense star clusters in producing triple systems of all possible component configurations. We use a grid of 148 independent cluster simulations (presented in Kremer et al. 2020),⁷ run using CMC (for Cluster Monte Carlo code), which covers roughly the complete range of GCs observed at present in the Milky Way. We systematically explore the dependence on initial virial radii (and subsequent BH dynamics) for clusters of various masses, metallicities, and locations within the Galactic tidal field. We analyze the origin of triples assembled in dense star clusters as a function of the clusters' initial properties, describe the triple demographics, as well as the production of mergers, transients, and GW sources.

The paper is organized as follows. In Section 2, we describe the numerical method used to evolve our cluster models. In Section 3, we analyze the origin of triple systems in star clusters, while in Section 4 we describe their demographics and general properties. In Section 5, we estimate the transient and GW phenomena as a result of the LK mechanism. Finally, in Section 6, we discuss the implications of our findings and lay out our conclusions.

2. Methods

Here we summarize the methods we use to evolve our population of clusters. For a detailed description see Kremer et al. (2020).

We use CMC, a Hénon-type Monte Carlo code (Hénon 1971a, 1971b; Joshi et al. 2000, 2001; Fregeau et al. 2003; Chatterjee et al. 2010, 2013; Pattabiraman et al. 2013; Rodriguez et al. 2015). CMC incorporates the physics relevant to both the overall evolution of the cluster properties and the specific evolution of the stars and compact objects therein.

The main process that shapes the evolution of global properties of clusters is two-body relaxation (e.g., Heggie & Hut 2003). In CMC, this is implemented by using the Hénon orbit-averaged Monte Carlo method (Joshi et al. 2000). To account for the fact that dense star clusters are subject to the tidal field of their host galaxy, we adopt an effective tidal massloss criterion that matches the tidal mass loss found in direct *N*-body simulations (Chatterjee et al. 2010).

Single and binary stars are evolved with the SSE and BSE codes, respectively (Hurley et al. 2000, 2002; Chatterjee et al. 2010), with up-to-date prescriptions for neutron star (NS) and BH formation (Fryer & Kalogera 2001; Vink et al. 2001; Belczynski et al. 2002; Hobbs et al. 2005; Morscher et al. 2015;

Rodriguez et al. 2016). In particular, two scenarios are considered for NS formation: iron core-collapse supernovae and electron-capture supernovae (Ye et al. 2019). In our simulations, the former receive natal kicks drawn from a Maxwellian with dispersion $s = 265 \text{ km s}^{-1}$, the latter with dispersion 20 km s^{-1} . Updated prescriptions for pulsar formation and evolution are also implemented (see Ye et al. 2019, for details). BHs are assumed to be formed with mass fallback and receive natal kicks by sampling from the same distribution used for NSs, but with kicks reduced in magnitude according to the fractional mass of fallback material (Fryer et al. 2012; Morscher et al. 2015). We also include prescriptions to account for pulsational-pair instabilities and pair-instability supernovae (Belczynski et al. 2016).

Binary–single and binary–binary strong encounters are integrated using Fewbody (Fregeau et al. 2004; Fregeau & Rasio 2007), with the addition of gravitational radiation reaction for all encounters involving BHs (Rodriguez et al. 2018a, 2018b). Collisions between stars during close encounters are treated in the sticky-sphere approximation, i.e., any pair of stars that pass close to one another are assumed to physically collide whenever their closest approach is smaller than the sum of their radii. Finally, we also take into account binary assembly through three-body-binary formation for every object (Aarseth & Heggie 1976; Heggie & Hut 2003; Morscher et al. 2015) and GW capture for two-body interactions involving BHs (Samsing et al. 2019).

2.1. Cluster Models

We use a set of 148 independent cluster simulations. We consider different total numbers of particles (single stars plus binaries; $N = 2 \times 10^5$, 4×10^5 , 8×10^5 , 1.6×10^6 , and 3.2×10^6), initial cluster virial radius ($r_v/pc = 0.5$, 1, 2, 4), metallicity (Z/Z = 0.01, 0.1, 1), and galactocentric distance ($R_{gc}/kpc = 2$, 8, 20).

We assume that all the models are initially described by a King profile, with initial King concentration parameter $W_0 = 5$ (King 1962). Stellar masses are drawn from a canonical Kroupa (2001) initial mass function in the range $0.08-150\,M$. The primordial stellar binary fraction is fixed to $f_b = 5\%$, with secondary masses drawn from a uniform distribution in mass ratio (e.g., Duquennoy & Mayor 1991). Binary orbital periods are sampled from a log-uniform distribution (e.g., Duquennoy & Mayor 1991), with the orbital separations ranging from near contact to the hard/soft boundary, while binary eccentricities are drawn from a thermal distribution (e.g., Heggie 1975).

Each simulation is evolved to a final time $T_{\rm H} = 14 \, {\rm Gyr}$, unless the cluster disrupts or undergoes a collisional runaway process (Kremer et al. 2020).

Primordial triples are not included in our cluster simulations. However, during strong binary-binary encounters, stable hierarchical triple systems can be formed (Rasio et al. 1995). Limitations in CMC currently require these triples to be broken artificially at the end of the integration time step. Nevertheless, whenever a stable triple is formed, its properties are logged, including the masses, stellar types, radii, and the semimajor axes and eccentricities for the inner and outer orbits. Since we

⁷ https://cmc.ciera.northwestern.edu

⁸ Assuming a Milky Way–like galactic potential (e.g., Dehnen & Binney 1998).

Note that, since these triple systems are de facto destroyed in the Monte Carlo simulations, it is possible for the components of these triples to subsequently form new triple systems, when in reality they could survive for a significant period of time.

lack information regarding the mutual orientation of the two orbits, we sample their argument of periapsis ω_0 , cosine of the relative inclination $\cos I_0$, and orbital phases from a uniform distribution (Antonini et al. 2016). To average out over these uncertainties, we realize this procedure 10 times for each triple formed in each of the 148 clusters presented in Kremer et al. (2020).

3. Dynamical Origin of Triples

In this section, we discuss the relevant formation channels of triples in star clusters, the characteristics of their progenitors, the formation times, and the recoil kicks that triple systems are imparted at the moment of formation. We label the inner and outer semimajor of the formed triples $a_{\rm in}$ and $a_{\rm out}$, respectively, the inner and outer eccentricities $e_{\rm in}$ and $e_{\rm out}$, respectively, the mass of the components of the inner binary m_1 and m_2 ($m_2 < m_1$), the total mass of the inner binary $m_{\rm in} = m_1 + m_2$, and the mass of the outer component m_3 . The total mass of the triple is $m_{\rm t} = m_{\rm in} + m_3$, while the initial relative inclination of the inner and outer orbit is i_0 . We label the remaining object $m_{\rm s}$ (fourth object leaving the system after the binary–binary interaction).

3.1. Progenitors

We find from our simulations that the majority of triple systems (\sim 98.2% of the overall triple population) are formed as a result of binary–binary encounters. In general, the probability of binary–binary encounters is (Binney & Tremaine 2008)

$$G_{\text{bin-bin}} \sim n_{\text{bin}}^2 s v_{\text{disp}},$$
 (1)

where $n_{\rm bin}$ is the density of binaries, σ is the cross section, and $v_{\rm disp}$ is the velocity dispersion. Since $n_{\rm bin}$ is largest in the core, the typical binary–binary encounter occurs in the core of dense star clusters. Of all the binary–binary encounters, the ones that successfully create triples involve two binaries of quite disparate sizes. Here the tighter binary ejects a member of the wider binary and inserts itself, thus creating a stable hierarchical triple. The replaced object receives a dynamical recoil kick and is ejected from the encountering system, ¹⁰ while the captured one becomes the tertiary in the newly formed triple system.

We illustrate in Figure 1 the properties of binaries that lead to the formation of triple systems in binary-binary encounters for a cluster with initial number of stars $N = 8 \times 10^5$. The other initial cluster parameters are $r_v = 1$ pc, $r_g = 8$ kpc, $Z = 0.1 Z_{\odot}$. In the top panel, we show the maximum of the semimajor axes $(a_{b,1} \text{ and } a_{b,2})$ of the two binaries that undergo the binary-binary encounter as a function of the minimum of them. We also overplot the probability density contours. We find that the bulk of the interactions that produce a triple include two binaries, of which one is wider than the other by \sim 2 orders of magnitude. This confirms our picture, where triples typically form when a binary replaces one of the components of a wider binary. We also show in Figure 1 (middle panel) the maximum eccentricities of the two binaries undergoing the binary-binary encounters $(e_{b,1}$ and $e_{b,2})$ as a function of the minimum of them. Since encounters thermalize the distribution of the eccentricities of the progenitors

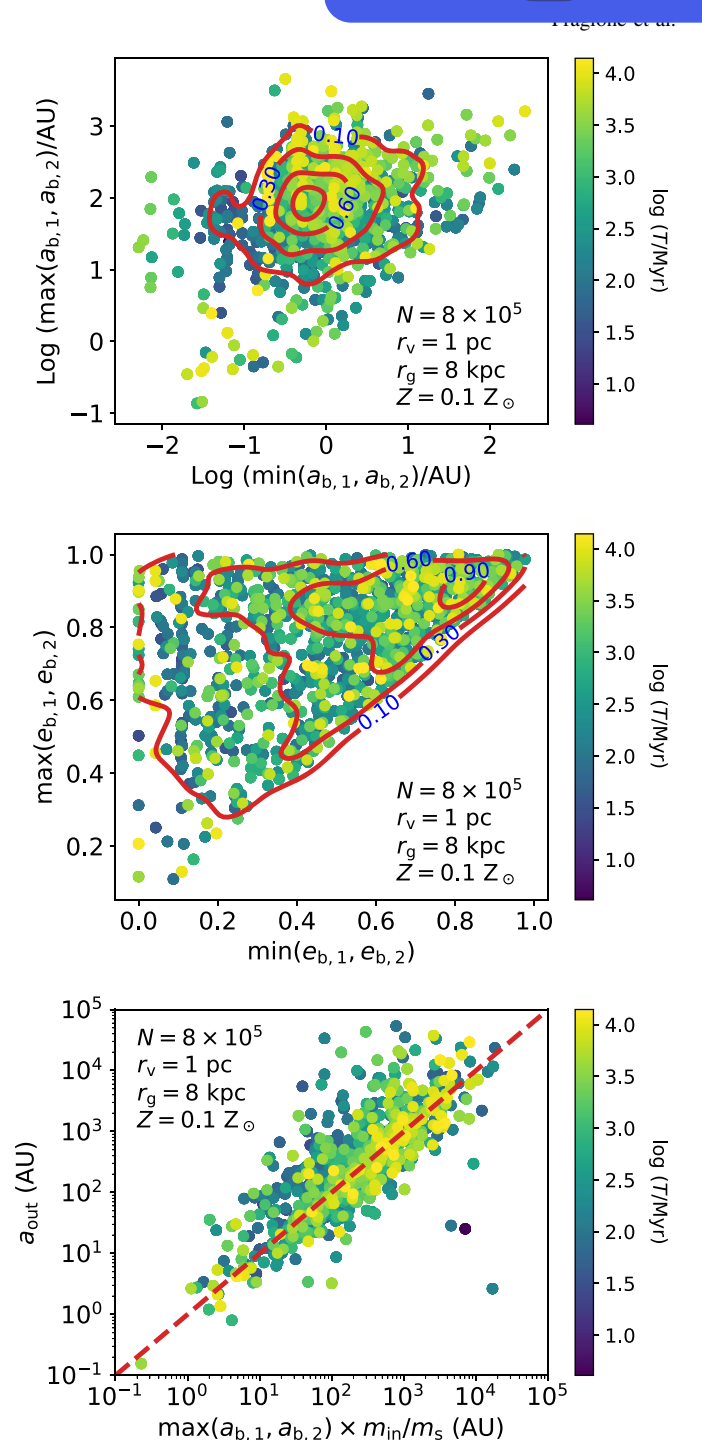


Figure 1. Properties of binaries that lead to the formation of triple systems in binary–binary encounters for a cluster with initial number of stars $N=8\times10^5$ ($r_{\rm v}=1~{\rm pc}$, $r_{\rm g}=8~{\rm kpc}$, $Z=0.1~Z_{\odot}$). Semimajor axes (top panel), eccentricities (middle panel), and outer semimajor axis as a function of the orbital elements of the binaries in the encounter (bottom panel) are shown. In the top two panels, the solid red lines represent the density contours of 10%, 30%, 60%, and 90% probability regions. The dashed red line in the bottom panel represents the x=y line. The color map represents log formation time.

(Heggie 1975), most of the binaries that produce triples are highly eccentric.

Since the typical triple-producing binary-binary encounter involves a tight binary exchanging into a wide binary, we expect the outer semimajor axis distribution of the outer semimajor axis of the triples to be related to the orbital

 $[\]overline{^{10}}$ In some cases, its recoil velocity would be high enough to eject it from the cluster (see Section 3.4).

Trial Version Wondershare PDFelement

elements of the ionized binaries. From energy conservation,

$$\frac{m_{\rm in}m_3}{a_{\rm out}} \sim \frac{m_3m_{\rm s}}{\max(a_{\rm b_1}, a_{\rm b_2})},$$
 (2)

where m_s is the mass of the replaced component in the wider binary (Sigurdsson & Phinney 1993). Therefore, the outer semimajor axis of the triple is linearly related to the semimajor axis of the wider binary through

$$a_{\text{out}} \sim \frac{m_{\text{in}}}{m_{\text{s}}} \max(a_{\text{b}_1}, a_{\text{b}_2}).$$
 (3)

We show this in the bottom panel of Figure 1. As expected, the majority of the systems lie on the x=y line. Triples that are outliers with respect to this simple scaling are systems formed during resonant encounters, where the energy is redistributed in a more complex way during multiple passages and interactions among the four objects (two binaries) involved in the encounter.

3.2. Cluster and Triple Properties

The initial conditions of the parent cluster set the distribution of the orbital elements of the formed triple systems. We show this in Figure 2, where we plot the cumulative distribution functions of inner and outer semimajor axes of triples in clusters of various initial numbers of stars, virial radii, and metallicities.

In the top panel of Figure 2, we illustrate the cumulative distribution function of triples in clusters with different initial numbers of stars ($N=2\times10^5-3.2\times10^6$) and $r_{\rm v}=2\,{\rm pc}$, $Z=0.01\,Z$, and $r_{\rm g}=20\,{\rm kpc}$. Triples that form in larger clusters tend to have smaller inner and outer semimajor axes. We find that ~50% of the systems have $a_{\rm in}/{\rm au}\lesssim (0.6, 1, 2, 4, 5)$ and $a_{\rm out}/{\rm au}\lesssim (1, 2, 4, 7, 10)\times10^2$ for $N=(32, 16, 8, 4, 2)\times10^5$, respectively. This comes from the fact that binaries that undergo binary–binary scattering and produce a triple system are tighter in more massive clusters. In these environments, stellar densities are typically higher than in less massive clusters and wide binaries are ionized by encounters with stars and compact objects.

We plot in the middle panel of Figure 2 the cumulative distribution function of triples in clusters of different initial virial radii $r_{\rm v}/{\rm pc}$ Î [0.5, 4] and $N=8\times 10^5$, $r_{\rm g}=8$ kpc, and Z=0.01 Z. Triples that form in clusters with larger virial radii tend to have wider inner and outer orbits. We find that $\sim 50\%$ of the triple systems have $a_{\rm in}/{\rm au}$ (0.3, 1, 2, 4) and $a_{\rm out}/{\rm au}$ (70, 250, 400, 700) for $r_{\rm v}/{\rm pc}=(0.5, 1, 2, 4)$, respectively. This is expected since clusters with smaller values of $r_{\rm v}$ typically have a higher density and velocity dispersion. Thus, the progenitor binaries (which later undergo binary–binary encounter to form triples) have to be more compact in order to remain bound after encounters with stellar or compact objects.

Finally, in the bottom panel of Figure 2, we plot the cumulative distribution function of triples in clusters of different initial metallicities $Z/Z=(0.01,\,0.1,\,1)$, with $N=8\times 10^5$, $r_{\rm v}=2$ pc, and $r_{\rm g}=20$ kpc. Triples that form in higher-metallicity clusters tend to have smaller inner and outer semimajor axes. We find that $\sim 50\%$ of the triple systems have $a_{\rm in}/{\rm au}\lesssim (2,\,2,\,0.7)$ and $a_{\rm out}/{\rm au}\lesssim (400,\,400,\,250)$ for $Z/Z=(0.01,\,0.1,\,1)$, respectively. This can be related to the

BH-burning process (Kremer et al. 2019e). BHs in metal-rich clusters are low mass and do not inject as much energy into the BH-burning process as BHs in metal-poor clusters. Thus, these clusters typically have higher densities and dispersion velocities. As a result, metal-poor clusters allow wider binaries to form triples compared to metal-rich clusters.

3.3. Cluster Properties and Formation Times

Triple systems are not formed uniformly in time. Rather, they track the evolutionary paths of the parent cluster. The clock of a star cluster is essentially set by its half-mass relaxation time (Spitzer 1987)

$$t_{\rm rh} \sim \frac{N^{1/2} r_{\rm v}^{3/2}}{2 \sin(N)^2 G^{1/2} \ln L},$$
 (4)

where $\frac{\partial n}{\partial t}$ is the average mass in the cluster and lnL is the Coulomb logarithm. As discussed in greater detail in Kremer et al. (2019a), the initial cluster size, set by its initial virial radius, is the key parameter that determines the ultimate fate of a cluster and its BH population ("BH-burning" mechanism). Clusters with smaller initial r_v have shorter relaxation times and have a dynamical clock that runs faster compared to clusters born with larger initial virial radius. These clusters could eject the majority of their BH population over their lifetime and appear as core-collapsed clusters.

In Figure 3, we plot the formation time (t_{form}) of triples in clusters of various initial numbers of stars, virial radii, and metallicities (same as Figure 2).

In the top panel, we show the cumulative distribution function of triples in clusters of different initial numbers of stars $N\,\hat{1}\,$ [2' $10^5, 3.2$ 10^6], $r_{\rm v}=2\,{\rm pc}, Z=0.01$ Z, and $r_{\rm g}=20\,{\rm kpc}.$ As expected from Equation (4), larger star clusters have longer evolutionary timescales. Hence, triples are assembled through binary–binary scatterings later compared to smaller clusters. We find that $\sim\!50\%$ of the triples are assembled at $t_{\rm form}\lesssim0.2\,{\rm Gyr}$ ($\sim\!0.25\,t_{\rm rh}$) for $N=2\times10^5,$ while $\sim\!50\%$ of the triples are assembled at $t_{\rm form}\lesssim2\,{\rm Gyr}$ ($\sim\!0.5\,t_{\rm rh}$) for $N=3.2\times10^6.$

We plot in the middle panel of Figure 3 the cumulative distribution function of triples in clusters of different initial virial radii $r_{\rm v}/{\rm pc}$ Î [0.5, 4], $N=8\times10^5$, Z=0.01~Z, and $r_{\rm g}=8~{\rm kpc}$. As discussed, the initial cluster size sets the dynamical clock of a stellar cluster. Among the four represented clusters, the ones with $r_{\rm v}=0.5~{\rm pc}$ and $r_{\rm v}=1~{\rm pc}$ are core collapsed (see Figure 5 in Kremer et al. 2020). Clusters with small initial virial radii form most of the triple systems much more quickly than clusters with larger initial sizes.

Finally, in the bottom panel of Figure 3, we show the cumulative distribution function of triples in clusters of different initial metallicities Z/Z $\hat{1}$ [0.01, 1], $N=8\times10^5$, $r_{\rm v}=2$ pc, and $r_{\rm g}=20$ kpc. Star clusters with lower metallicities form more massive BHs than clusters with higher metallicities (see Figure 1 in Kremer et al. 2020). These more massive BHs undergo dynamical friction on a shorter timescale and therefore start the assemble of triple systems earlier.

3.4. Recoils and Ejections

Binary-binary exchange encounters impart recoil kicks to any triples they produce. Leigh et al. (2016) showed that the ejection velocity of the single escaper (m_s) in such an encounter

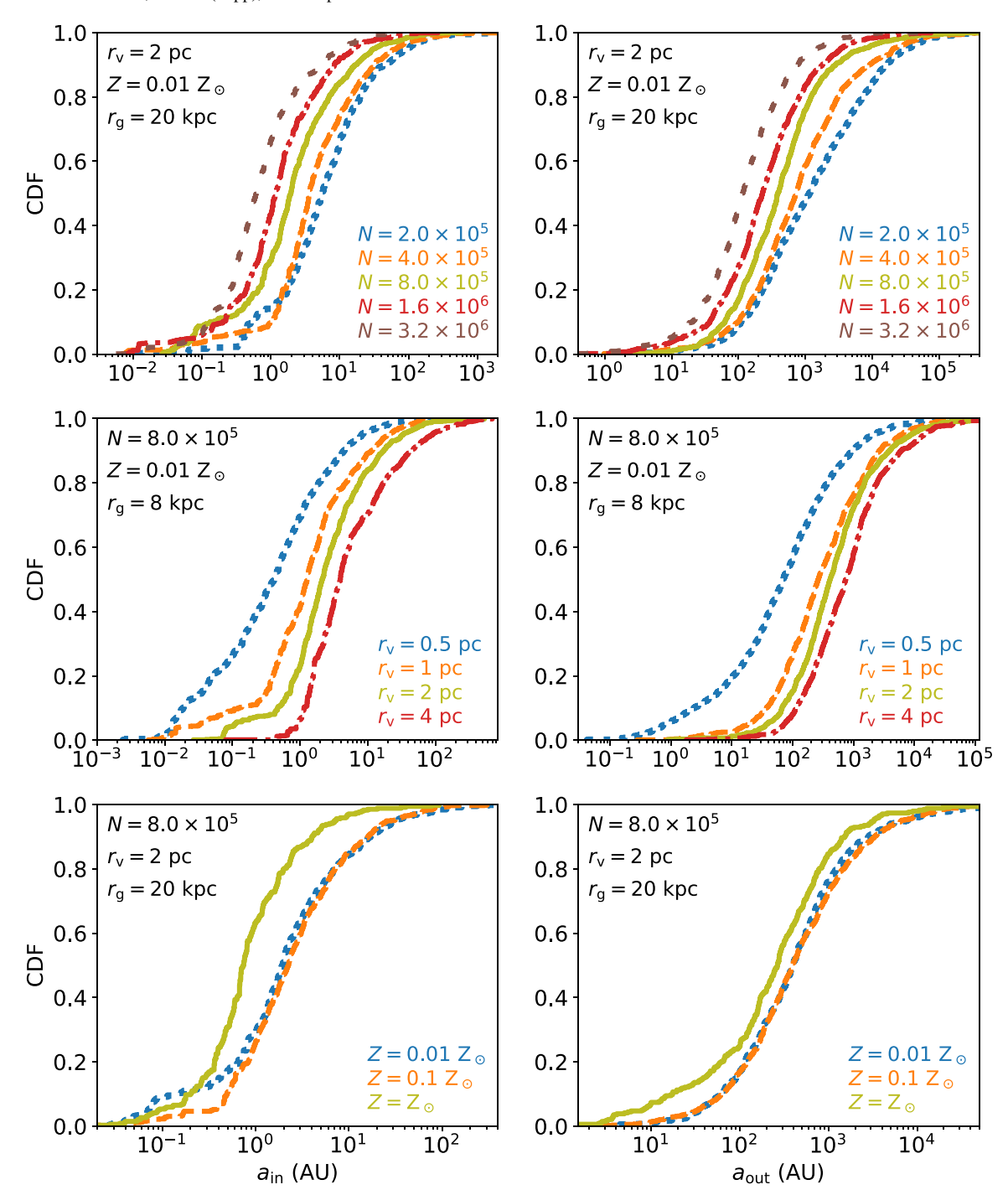


Figure 2. Cumulative distribution functions of inner $(a_{in}; left panels)$ and outer $(a_{out}; right panels)$ semimajor axis of triples in clusters of various initial numbers of stars (top panels), virial radii (middle panels), and metallicities (bottom panels).

is well described by the distribution¹¹

$$f(v_{\rm ej,s})dv_{\rm ej,s} = \frac{3|E|^2 \quad v_{\rm ej,s}}{\left(|E| + \frac{1}{2} \quad v_{\rm ej,s}^2\right)^3} dv_{\rm ej,s},\tag{5}$$

where

$$=\frac{m_s(m_s+m_{\rm in})}{m_{\rm in}}\tag{6}$$

and |E| is the total initial energy. From the conservation of linear angular momentum, the recoil velocity of the triple is

$$v_{\rm rec} = \frac{m_s}{m_s} v_{\rm ej,s}.$$
 (7)

This recoil kick can be large enough to eject the triple from the core (where it will eventually sink back as a result of dynamical friction) or even from the cluster.

We use the data recorded on binary–binary scatterings that lead to the formation of stable triple systems during the cluster's lifetime to compute $\nu_{\rm rec}$. In Figure 4, we show the recoil velocity

¹¹ This assumes that the initial angular momentum is negligible. For a general discussion, see Valtonen & Karttunen (2006).

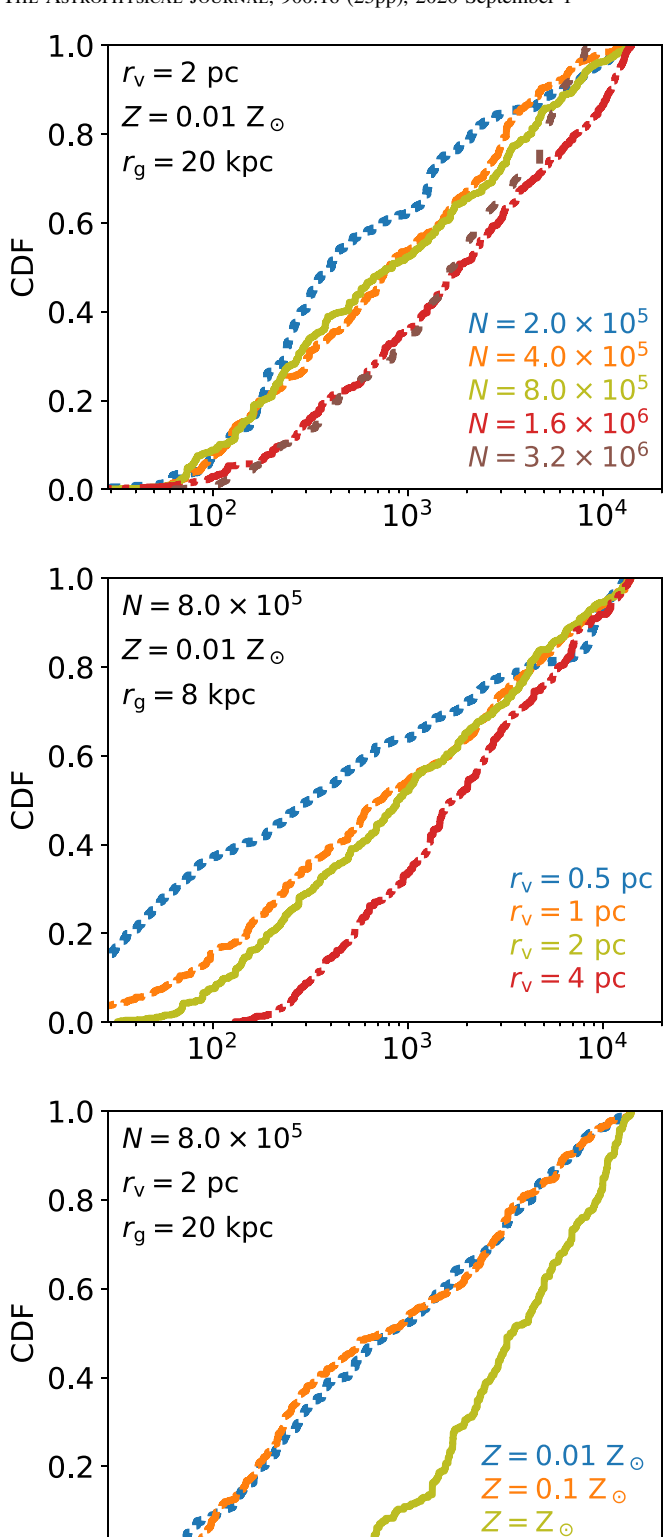


Figure 3. Formation time (t_{form}) of triples in clusters of various initial numbers of stars (top panel), virial radii (middle panel), and metallicities (bottom panel).

 10^{2}

10³

 t_{form} (Myr)

0.0

 $v_{\rm rec}$ of the triple systems assembled in the cores of star clusters of various initial N (for fixed $r_{\rm v}=2\,{\rm pc},\ r_{\rm g}=20\,{\rm kpc},\ {\rm and}\ Z=0.01\,Z_{\odot}$) as a function of the cluster escape speed $v_{\rm esc}$ at the moment of formation. For these clusters, we find that $\lesssim 1\%$ of the

formed triples could escape the clusters owing to dynamical recoil kicks (if they do not encounter other stars or compact objects). Moreover, the escaping systems tend to be ejected from the cluster at later times, when the cluster escape speed decreases to lower values. Most of the triples will not leave the cluster. Rather, they will be kicked on elongated orbits out of the cluster core. As they are more massive than the average star, they would sink back to the cluster core on a dynamical friction timescale

$$t_{\rm df} \sim \frac{\acute{a}m\,\tilde{\mathsf{n}}}{m_{\rm t}}t_{\rm rh},\tag{8}$$

where $m_{\rm t}=m_{\rm in}+m_3$ is the total mass of the triple.

4. Demographics

In this section, we discuss how the parent cluster initial conditions shape the orbital properties of the formed triples and describe their demographics.

We are interested in triples that are hierarchically stable. While simulating strong encounters inside CMC, triple stability is checked using the stability criteria given by Mardling & Aarseth (2001),

$$\frac{a_{\text{out}}}{a_{\text{in}}} \left(e_{\text{out}}, \frac{m_{\text{out}}}{m_{\text{in}}} \right) \quad 2.8, \tag{9}$$

where

$$\left(e_{\text{out}}, \frac{m_{\text{out}}}{m_{\text{in}}}\right) = \left[\left(1 + \frac{m_{\text{out}}}{m_{\text{in}}}\right) \frac{1 + e_{\text{out}}}{\sqrt{1 - e_{\text{out}}}}\right]^{2/5}$$

$$\left(1 - e_{\text{out}}\right) \left(1 - \frac{0.3 i_0}{180}\right). \tag{10}$$

We subdivide the triple population into four categories, such that the stellar types of the two components k_1 and k_2 of the inner binary (see Hurley et al. 2000) are always $k_1 \le k_2$:

- 1. triples with a main-sequence (MS) star in the inner binary;
- 2. triples with a giant (G) star in the inner binary;
- 3. triples with a WD in the inner binary;
- 4. triples with an NS or BH in the inner binary.

Among the systems with an inner BH-BH binary, we also consider triples where all the components are BHs, which we label BH-BH-BH.

As a general trend, we find that a cluster typically assembles hundreds of triples with an inner BH-BH binary (of which \sim 70%–90% have a BH as tertiary) or an inner MS–BH binary. Additionally, tens of triples with an inner MS-MS or WD-BH are produced. However, only clusters with $r_v \leq 1$ pc efficiently assemble triples with an inner binary composed of an MS-WD or WD-WD and produce ~10 times more systems with an inner MS-MS binary. Again, this is a natural consequence of the BH-burning process (Kremer et al. 2019e), since only clusters with small initial virial radii are able to eject most of their BH population, thus allowing lighter objects to sink to their innermost regions and efficiently produce triples. Moreover, we find that $\sim 50\%$ of the overall triple population from our simulations consists of systems where all the components are BHs. Roughly 10% of the systems take the form of a binary BH with a non-BH tertiary and \sim 38% take the form of an inner binary with at least one MS star. Other triples constitute the remaining $\sim 2\%$. Tables A1-A2 summarize all the different

 10^{4}

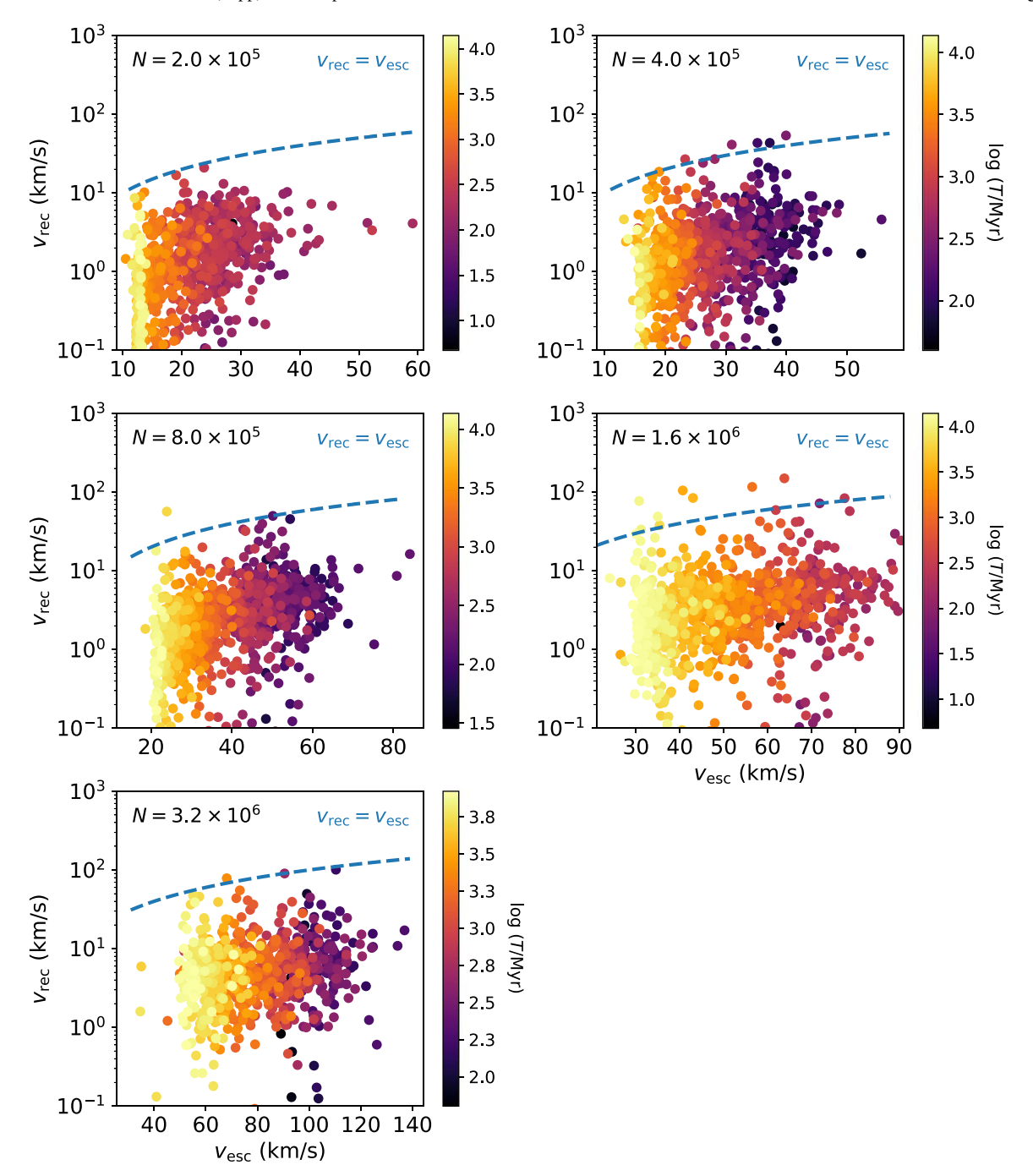


Figure 4. Recoil velocity $v_{\rm rec}$ of the triple systems assembled in the cores of star clusters of various initial numbers of stars $N(r_{\rm v}=2~{\rm pc},r_{\rm g}=20~{\rm kpc},Z=0.01~{\rm Z_{\odot}})$, as a function of the cluster escape speed $v_{\rm esc}$ at the moment of formation. The dotted-dashed blue line represents $v_{\rm rec}=v_{\rm esc}$. Color code: log formation time.

triples formed in each cluster simulation in our ensemble, subdivided into the above-described categories.

4.1. Gravitational Wave Captures and Mergers during Triple Formation

A handful of triple systems (\sim 0.1% of the overall population) are formed during binary–single encounters as a result of GW captures (Samsing et al. 2019). In this process, the single has the chance to pass sufficiently close to the binary to dissipate some energy via GW radiation, thus remaining bound to the binary itself. For all triples assembled this way in our simulations, we show in Figure 5 the outer mass as a function of the inner binary's

total mass. We find that the binary that intervenes in the process, which later becomes the inner binary of the triple, is always a binary BH. The majority of the triples formed through GW captures are made up of three BHs, while a few systems have a star (either MS or G) or WD as the outer companion. We find no GW capture systems with an NS outer companion.

During the binary-binary encounters that produce a triple system, two of the objects can pass close enough to merge. This can occur in multiple ways: collision and merger of two stars (MS or G), tidal disruption of stars by a compact object, and merger of two compact objects. In Figure 6, we plot for all simulations the masses of the components (m_{1m} and m_{2m}) that merge during binary-binary encounters that yield triples

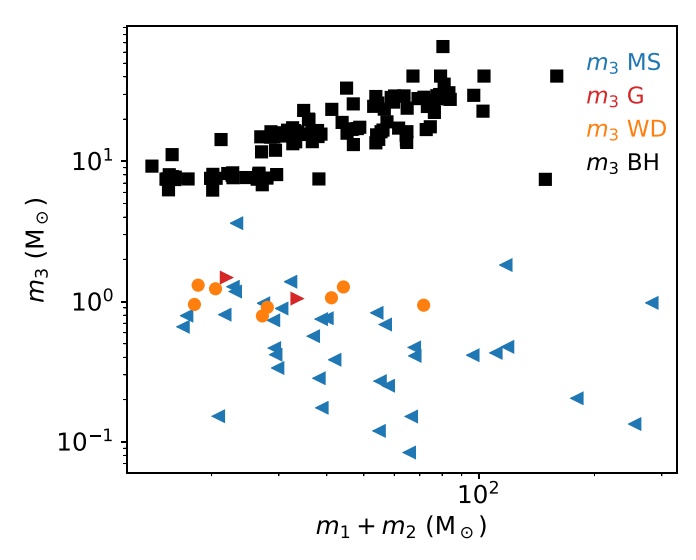


Figure 5. Outer mass as a function of the total mass of the inner binary of the triple systems that form through GW captures during binary–single encounters. The binary, which becomes the inner binary of the triple, is always a binary BH.

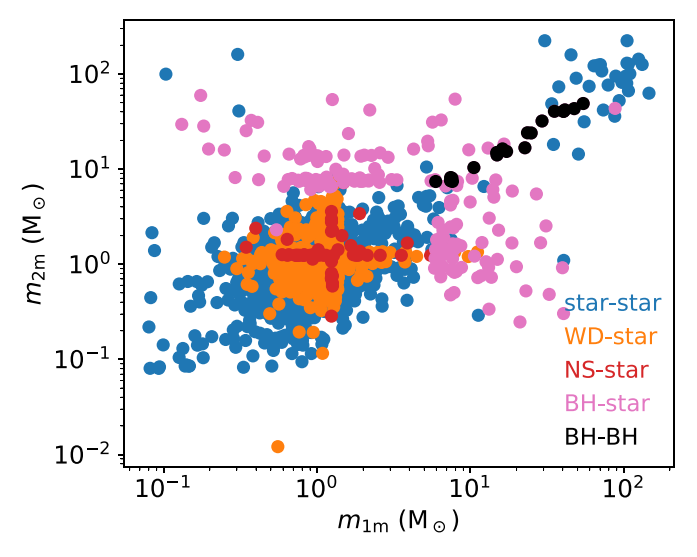


Figure 6. Masses of the components (m_{1m} and m_{2m}) that merge during binary-binary encounters that lead to triple formation. Different colors represent different stellar and compact-object types.

 $(\sim 1.7\%$ of their overall population). Different colors represent different stellar and compact-object types. Among the stars that collide, we find that $\sim 90\%$ and $\sim 10\%$ of the mergers are with MS or G stars, respectively. In the standard scenario for triple formation, the tighter binary ejects the single star it replaces, but no ejection occurs in this process.

4.2. Stability and Softness

We define the softness parameter (Heggie 1975)

$$h^{\circ} \frac{Gm_{\rm in}m_3}{2a_{\rm out}\acute{a}m\,\tilde{n}_{\rm disp}^2},\tag{11}$$

where $\acute{a}n\tilde{n}$ and $v_{\rm disp}$ are the average mass in the cluster and the cluster velocity dispersion, respectively. Triples that have $\eta \ll 1$ are referred to as "soft" and will become even softer on average, until they are disrupted by the background population.

Triples with $\eta \gg 1$ are referred to as "hard" and tend to become even harder by interacting with cluster stars (Heggie 1975).

We illustrate in the left panels of Figure 7 the probability distribution function of the ratio of the outer and inner semimajor axes of all triple populations formed in our 148 cluster simulations. We find that the majority of the systems have $a_{\rm out}/a_{\rm in}\gtrsim 10$, regardless of the composition of the inner binary. We also show in Figure 7 the probability distribution function of the softness parameter η (right panels) of all triples formed in the simulations. We find quite generally that triple populations have $\eta\gg 1$, with only a small tail of soft triples and a main peak at $\eta\sim 100$.

4.3. Formation Time, Inner Mass Ratio, Outer Mass Ratio

We show in Figure 8 the probability distribution function of the formation time (left), the inner mass ratio (middle), and the outer mass ratio (right) of all the triple populations formed in the simulations.

As a common trend, we find that triples whose inner binary has at least one BH typically form on a shorter timescale compared to other triples. This can be understood in terms of the BH-burning mechanism (Kremer et al. 2019e). In this process, strong dynamical encounters between the BHs act as an energy source for the rest of the cluster. Thus, BHs tend to occupy the innermost and densest parts of the cluster, where most of the binary–binary interactions take place, preventing other components from efficiently segregating there. As a result, triples whose inner binary does not contain a BH tend to form on longer timescales, when most of the BHs have been processed and have left the cluster.

For MS stars, we define the inner mass ratio $m_{\rm MS}/m_{\rm comp}$ as the ratio between the MS star's mass $(m_{\rm MS})$ and that of its companion $(m_{\rm comp})$. If there are two MS stars in the inner binary, we define the inner mass ratio as $m_{\rm MS,2}/m_{\rm MS,1}$, with $m_{\rm MS,1} > m_{\rm MS,2}$. The same applies to G stars, WDs, NSs, and BHs. The outer mass ratio is simply defined as the ratio between the total mass of the inner binary and the mass of the tertiary. Interestingly, we find that the inner mass ratio is usually peaked at ~ 1 , unless the system only has one BH in the inner binary. The distribution of outer mass ratios is also nearly peaked at ~ 1 , except for systems with an inner binary composed of an MS–MS, MS–BH, WD–BH, or NS–BH. The secondary peaks at ~ 10 –100 corresponds to a low-mass stellar tertiary.

4.4. Survivability

In the dense stellar environment of star clusters, triple systems may be perturbed through encounters with other passing objects. Such encounters will alter the orbital properties of the triple significantly or even disrupt it. This process happens on a typical timescale ¹² (Binney & Tremaine 2008; Ivanova et al. 2008)

$$T_{\text{enc}} = 8.5 \text{ '} 10^{12} \text{ yr } P_{\text{out,d}}^{-4/3} m_{\text{trip}, M}^{-2/3} s_{10 \text{ km s}^{-1}}^{-1} n_{10^5 \text{ pc}^{-3}}^{-1}$$

$$\text{'} \left[1 + 913 \frac{m_{\text{trip}, M} + \acute{a} m \tilde{n}_{M}}{2P_{\text{out,d}}^{2/3} m_{\text{trip}, M}^{1/3} s_{10 \text{ km s}^{-1}}^{-1}} \right]^{-1}, \tag{12}$$

where P_{out} is the orbital period of the outer orbit and $\acute{a}m\tilde{n}$ is the average stellar mass in the cluster.

 $[\]overline{12}$ Quantities x_a are expressed with physical units u as $x_{a,u} \circ x_a/u$, so that $x_{a,u}$ is dimensionless.

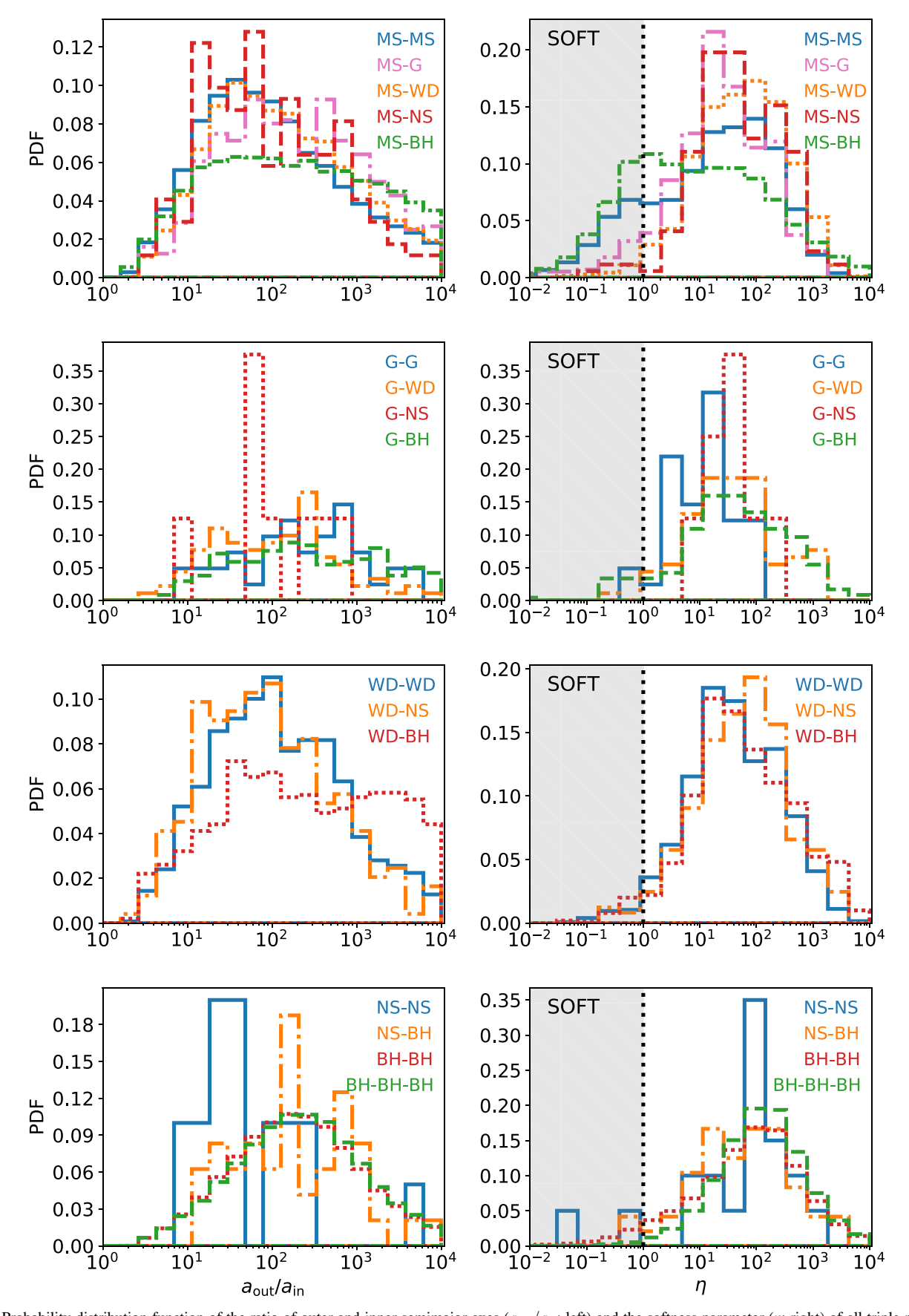


Figure 7. Probability distribution function of the ratio of outer and inner semimajor axes $(a_{out}/a_{in}; left)$ and the softness parameter $(\eta; right)$ of all triple populations formed in our 148 cluster simulations. Top row: triples with an MS star plus a companion in the inner binary. Second row: triples with a G star plus a companion in the inner binary. Third row: triples with a WD plus a companion in the inner binary. Bottom row: triples with an NS or BH plus a companion in the inner binary.

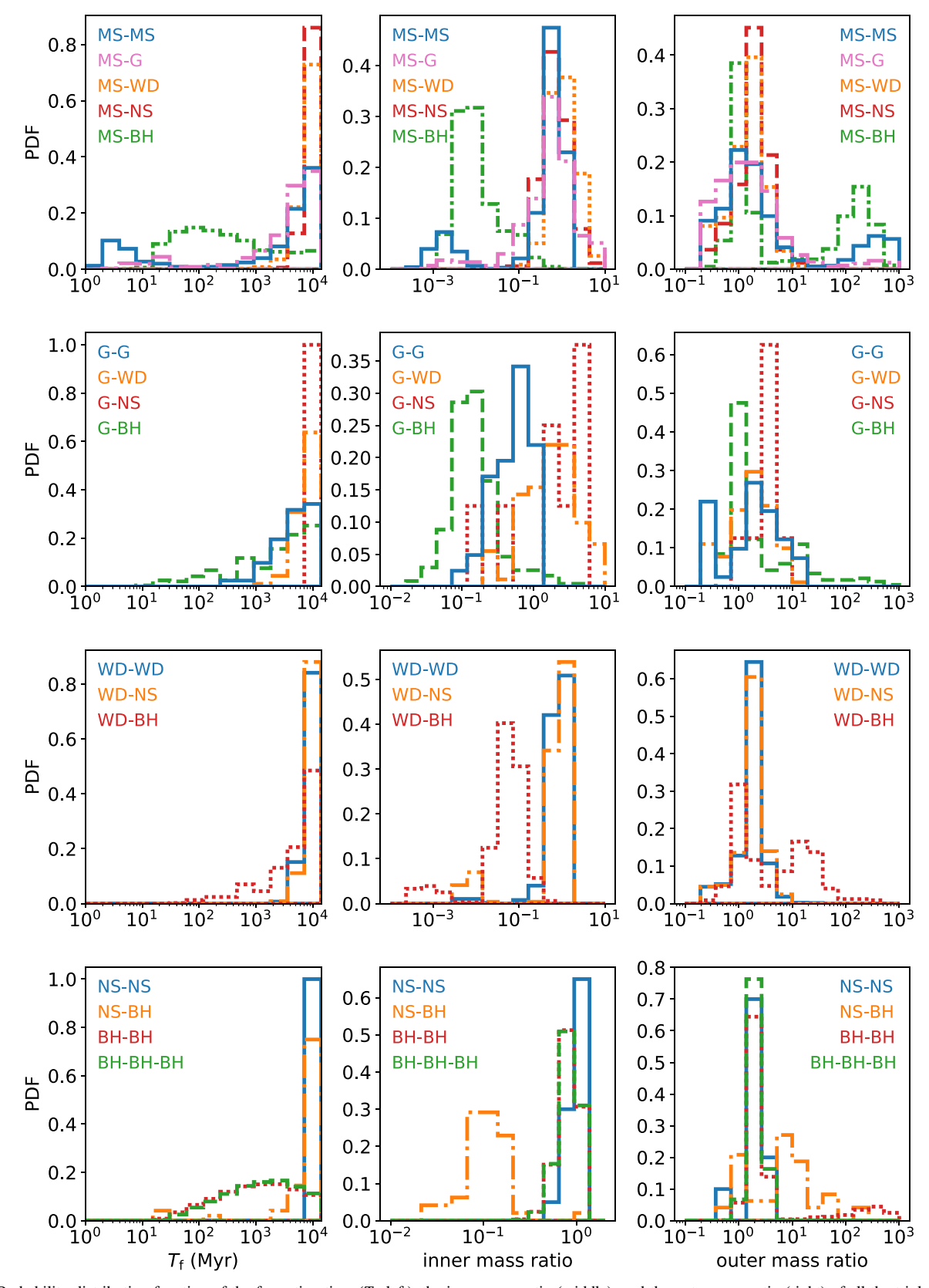


Figure 8. Probability distribution function of the formation time (T_f , left), the inner mass ratio (middle), and the outer mass ratio (right) of all the triple populations formed in our 148 cluster simulations. Top row: triples with an MS star plus a companion in the inner binary. Second row: triples with a G star plus a companion in the inner binary. Third row: triples with a WD plus a companion in the inner binary. Bottom row: triples with an NS or BH plus a companion in the inner binary.

We show in Figure 9 all late-time snapshots (10–13 Gyr) for model clusters compared to Milky Way clusters. The latter are taken from Baumgardt & Hilker (2018) and represented such

that their size is proportional to the integrated *V*-band magnitude of each cluster (Harris 1996). Thus, larger symbols denote clusters that are best observed. In color code, we

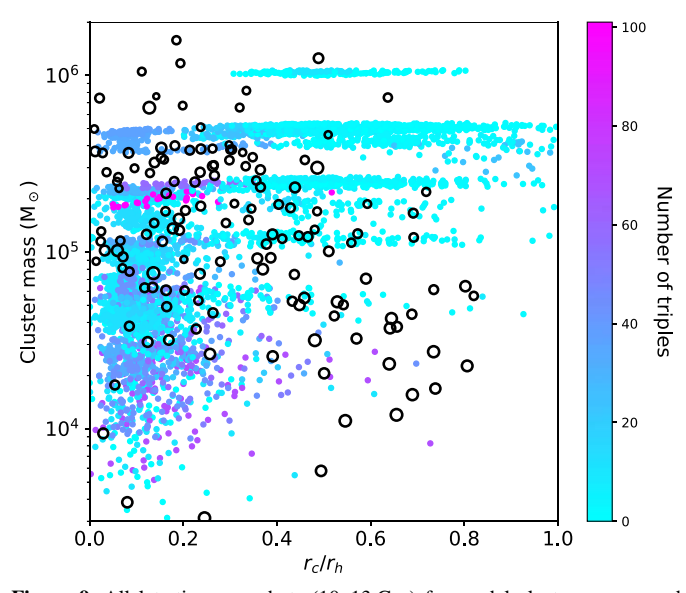


Figure 9. All late-time snapshots (10–13 Gyr) for model cluster masses and concentrations (colored points). Milky Way clusters (black points) are taken from Baumgardt & Hilker (2018), with the size of each black point corresponding to the integrated *V*-band magnitude of each cluster (Harris 1996; larger symbols denote clusters that are best observed). Color code: number of triples with at least one luminous component that survive at present day unperturbed in the cluster.

represent the number of triples with at least one luminous (observable) component that survive in the cluster, i.e., triples whose encounter timescales are long enough to remain unperturbed. We find that clusters are on average expected to host tens of luminous triples at present.

5. Triple-assisted Mergers: Transients and Gravitational Waves

In this section, we discuss the LK mechanism that takes place in triple systems. We then apply an analytical formalism to compute the maximum eccentricity attained by the triples formed in our simulations (subdivided as described in Section 4) and to infer the fraction of systems that result in a merger, a transient phenomenon, or GW emission by the LK mechanism.

5.1. Lidov-Kozai Mechanism

A triple system made up of an inner binary that is orbited by an outer companion undergoes LK oscillations in eccentricity whenever the initial mutual inclination of the inner and outer orbits is in the range 40 i_0 140 (Kozai 1962; Lidov 1962; quadrupole order of approximation). During these cycles, the eccentricity and inclination of the inner orbit can experience periodic oscillations on a secular quadrupole LK timescale

$$T_{\rm LK} = \frac{8}{15p} \frac{m_{\rm trip}}{M_3} \frac{P_{\rm out}^2}{P_{\rm in}} (1 - e_{\rm out}^2)^{3/2}.$$
 (13)

In the previous equation, $P_{\rm in}$ and $P_{\rm out}$ are the orbital periods of the inner and outer binaries, respectively. We note that the exact size of the LK inclination window depends also on the physical parameters of the three objects, thus varying from case to case (e.g., Grishin et al. 2018). On this typical timescale, the relative inclination of the inner orbit and outer orbit slowly increases while the orbital eccentricity of the inner orbit

decreases, and vice versa, conserving angular momentum (see Naoz 2016, for a review). The inner eccentricity can reach almost unity during LK cycles, which is typically achieved in the case $i_0 \sim 90^{\circ}$.

Whenever the outer orbit is eccentric (octupole order of approximation), the inner eccentricity can reach almost unity even if the initial inclination lies outside of the window of $\sim\!\!40^\circ\!\!-\!\!140^\circ$ (Naoz et al. 2013). This happens over the octupole timescale

$$T_{\text{oct}} = \frac{1}{-}T_{\text{LK}},\tag{14}$$

where the octupole parameter is defined as

$$= \frac{m_1 - m_2}{m_1 + m_2} \frac{a_{\text{in}}}{a_{\text{out}}} \frac{e_{\text{out}}}{1 - e_{\text{out}}^2}.$$
 (15)

Nevertheless, LK cycles can be suppressed by additional sources of precession (e.g., Fabrycky & Tremaine 2007; Naoz et al. 2013), such as nondissipative tides, which operate on a timescale (Kiseleva et al. 1998; Eggleton & Kiseleva-Eggleton 2001)

$$T_{\text{tide}} = \frac{8a_{\text{in}}^{13/2}}{15(Gm_{\text{in}})^{3/2}} \frac{(1 - e_{\text{in}}^2)^5}{8 + 12e_{\text{in}}^2 + e_{\text{in}}^4}$$

$$\int \left[2\frac{m_2}{m_1}k_1R_1 + 2\frac{m_1}{m_2}k_2R_2\right]^{-1}, \tag{16}$$

where k_1 , R_1 and k_2 , R_2 are the apsidal motion constants and radii of the two stars in the binary (Hut 1981), respectively, or general relativistic (GR) precession, which operates on a typical timescale (Peters 1964)

$$T_{\rm GR} = \frac{a_{\rm in}^{5/2} c^2 (1 - e_{\rm in}^2)}{3G^{3/2} (m_1 + m_2)^{3/2}}.$$
 (17)

To compute the maximum eccentricity $e_{\rm max}$ attained by triples, we use the following equation to find the root of $j_{\rm min} = \sqrt{1-e_{\rm max}^2}$ (e.g., Liu et al. 2015):

$$\frac{3}{8} \cdot \left\{ e_0 + (j_{\min}^2 - 1) + (5 + 4j_{\min}^2) \right\}$$

$$\cdot \left[1 - \frac{((j_{\min}^2 - 1) Z_{\min} + e_0^2 Z_0 + 2j_0 \cos I_0)^2}{4j_{\min}^2} \right]$$

$$- (1 + 4e_0^2 + 5e_0^2 \cos^2 W_0) \sin^2 I_0 + G_R(j_0^{-1} - j_{\min}^{-1})$$

$$+ \frac{\text{Tide}}{15} \cdot \left(\frac{32 - 24j_0^2 + 3(1 + j_0^2)^2}{8j_0^9} \right)$$

$$- \frac{32 - 24j_{\min}^2 + 3(1 + j_{\min}^2)^2}{8j_{\min}^9} \right) = 0.$$
(18)

The above equation is derived in a quadrupole approximation but has been shown to remain approximately valid even when the octupole effect is nonnegligible (e.g., Anderson et al. 2016, 2017; Liu et al. 2019). In the previous equation, e_0 is the initial inner binary eccentricity, $j_0 = \sqrt{1 - e_0^2}$, $Z_{\min} = L(e = e_{\max})/L_{\text{out}}$, and $Z_0 = L(e = e_0)/L_{\text{out}}$, where L and L_{out} are the angular momenta of the inner and outer

Trial Version Wondershare PDFelement

binaries, respectively. The parameters

$$_{GR} = \frac{3Gm_{in}^2 a_{out}^3 (1 - e_{out}^2)^{3/2}}{c^2 a_{in}^4 m_{out}}$$
 (19)

 $\text{and}^{\color{red}13}$

$$_{\text{Tide}} = \frac{15m_{\text{in}}^2 a_{\text{out}}^3 (1 - e_{\text{out}}^2)^{3/2} k_{\text{Love}, *} R_*^5}{a_{\text{in}}^8 m_* m_{\text{out}}}$$
(20)

represent the relative strength of the apsidal precession due to GR and tidal bulge of the star.¹⁴ Here R_* and $k_{\text{Love},*}$ are the radius and the Love number of a given star, respectively. For an MS star, a good approximation is $k_{\text{Love},*} = 0.028$, while for other stellar types it depends on the details of the stellar structure (Hut 1981; Kiseleva et al. 1998).

Eccentricity excitations near unity during LK cycles can deeply alter the evolution of binary systems, the components of which would otherwise not interact if isolated from the tertiary perturber. For instance, inner binaries composed of stars can efficiently shrink their orbit owing to efficient tides at the pericenter (e.g., Perets & Fabrycky 2009; Naoz & Fabrycky 2014; Naoz et al. 2016; Stephan et al. 2016; Rose et al. 2019) or merge owing to dissipation of energy via GW emission (e.g., Stephan et al. 2016, 2019; Grishin et al. 2018; Hoang et al. 2018; Fragione et al. 2019b).

In a cluster's dense stellar environment, triple systems may be perturbed through encounters with other passing stars (Hamers 2018). As discussed, these encounters take place on a typical timescale $T_{\rm enc}$ (see Equation (12)). Such encounters can reset the triple by altering the orbital properties significantly. In the case of soft triples, encounters with other cluster members will even tend to disrupt it, on average. Thus, unlike triples in isolation, LK cycles must occur on timescales shorter than the encounter timescale. If $T_{\rm LK} < T_{\rm enc}$, the inner binary eccentricity can reach high values and trigger the interaction, or even the merger, of the components in the inner binary. If $T_{\rm LK} > T_{\rm enc}$, LK oscillations could be suppressed by stellar encounters (Antonini et al. 2016).

As an example, we show in Figure 10 a comparison between the LK timescale and the encounter timescale for triples with an MS star plus a companion in the inner binary: MS–MS (top left panel), MS–G (top right panel), MS–WD (middle left panel), MS–NS (middle right panel), and MS–BH (bottom left panel). In each panel, for the systems that satisfy $T_{\rm LK} < T_{\rm enc}$, we represent in color code the maximum eccentricity attained by triples, computed by using Equation (18).

We showed in Section 3 that triple systems experience a recoil kick as a result of the binary-binary exchange encounter. The recoil kick can be large enough to eject the triple from the core. If not ejected from the cluster, the triple would have a new elongated orbit with pericenter in the cluster core and apocenter in the cluster outskirts. The triple would eventually sink back to the core as a result of dynamical friction (Equation (8)). However, the encounter timescale of the triple would be longer than given by Equation (12) since it would spend most of its orbit in regions less dense than the core. To bracket the uncertainties, we show the results of our LK analysis both in

the case in which the encounter timescale of triples is computed using Equation (12) and in the case in which $T_{\rm enc}$ goes to infinity (essentially corresponding to a triple ejected from the cluster environment; see Section 3.4).

5.2. Collision and Accretion in Triples with a Main-sequence Star, a Giant, or a White Dwarf in the Inner Binary

During the LK evolution, the inner orbital eccentricity is excited, which can result in crossing of the Roche limit. Given a binary system with components m_i and m_j , we define the dimensionless number (Eggleton 1983)

$$m_{\rm i} = 0.49 \frac{(m_j/m_i)^{2/3}}{0.6(m_i/m_i)^{2/3} + \ln(1 + (m_i/m_i)^{1/3})}.$$
 (21)

Thus, the Roche limit is defined as

$$a_{\text{Roche,ij}} \circ \frac{R_{\text{j}}}{m_{\text{i}}},$$
 (22)

where R_j is the radius of m_j . The definition of $a_{\text{Roche,ji}}$ is obtained with the substitutions i j and j i. For triples that are composed of an MS star or a G star in the inner binary, we compute e_{max} from Equation (18) and define Roche lobe overflow to occur whenever (e.g., Stephan et al. 2019)

$$a(1 - e_{\text{max}}) \quad a_{\text{Roche}}. \tag{23}$$

We show in Figure 11 the probability distribution function of the ratio of the inner binary's pericenter during an LK cycle to the Roche semimajor axis (Equation (22)), for triples with an MS star or a G star in the inner binary. The shaded area represents the region where $a(1 - e_{\text{max}})/a_{\text{Roche}}$ 1, where a Roche lobe overflow can take place. According to the companion of the MS or G star in the inner binary of these triples, the LK cycles can produce either accretion or a physical merger. In the case of MS inner binaries, MS-MS and MS-G would likely form blue stragglers and rejuvenated giants, MS-WD would form cataclysmic variables, and MS-NS or MS-BH would give birth to X-ray binaries, millisecond pulsars, or Thorne-Zytkow objects. On the other hand, G-G mergers would form rejuvenated giants, while mergers of G with a compact object could give birth to ultracompact X-ray binaries (Hurley et al. 2000, 2002; Ivanova et al. 2010; Naoz et al. 2016; Perets et al. 2016; Kremer et al. 2018, 2019c; Fragione et al. 2019c; Stephan et al. 2019). In Figure 11, we also illustrate a comparison of the systems that satisfy $a(1 - e_{\text{max}})/a_{\text{Roche}}$ 1 when computing T_{enc} using Equation (12) (solid line) and when $T_{\rm enc}$ goes to infinity (dotted line). We find that there is not a significant difference between using Equation (12) to compute $T_{\rm enc}$ and treating $T_{\rm enc}$ as infinite, since for these systems the LK timescale is typically smaller than the encounter timescale from Equation (12).

We estimate that \sim 35%, 43%, 38%, 32%, and 14% of the triple systems merge with inner MS–MS, MS–G, MS–WD, MS–NS, and MS–BH binaries, respectively, while \sim 12%, 38%, 16%, and 15% of the systems merge for triples with inner G–G, G–WD, G–NS, and G–BH binaries, respectively. Assuming a GC density $\rho_{\rm GC}\sim 2.31\,{\rm Mpc}^{-3}$ (Rodriguez et al. 2015; Rodriguez & Loeb 2018), we estimate a merger rate of \sim 10⁻¹–10⁻² Gpc⁻³ yr⁻¹ for these populations of triples, consistent with the previous estimated rates in cluster binaries (Kremer et al. 2019c) and in field triples (Fragione et al. 2019c).

 $[\]overline{^{13}}$ This assumes that only one of the two objects in the inner binary raises tides. If both components of the inner binary raise tides, $\epsilon_{\rm Tide}$ has a contribution from both components.

¹⁴ We do not include precession due to rotational distortion of the star, which is usually negligible.

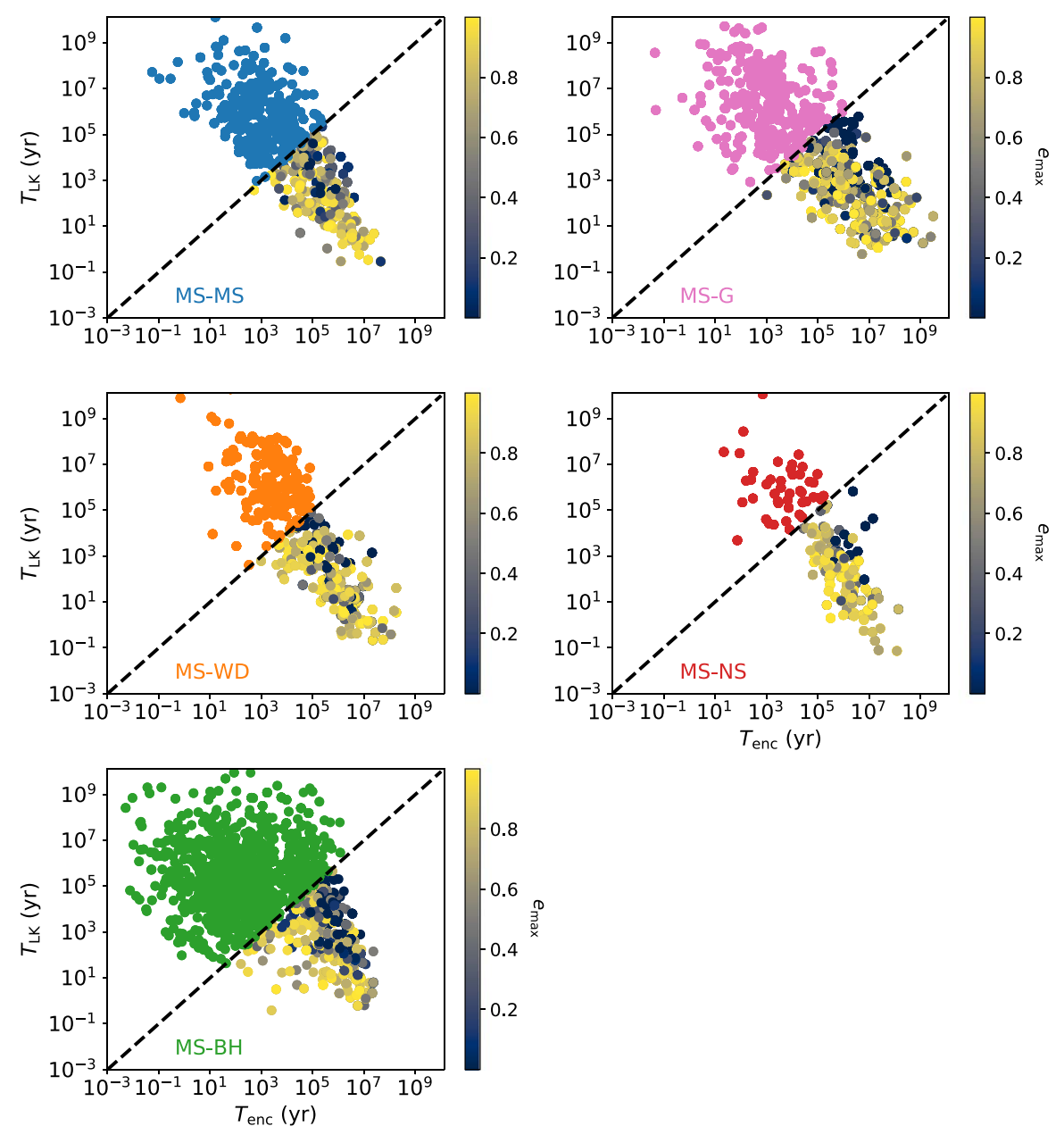


Figure 10. Comparison between the LK timescale (T_{LK}) and the encounter timescale (T_{enc}) for triples with an MS star plus a companion in the inner binary: MS–MS (top left panel), MS–G (top right panel); MS–WD (middle left panel), MS–NS (middle right panel), MS–BH (bottom left panel). Color code: maximum eccentricity attained by triples with $T_{LK} < T_{enc}$, computed using Equation (18).

In Figure 12, we plot the probability distribution function of the ratio of the inner binary's pericenter during an LK cycle to the Roche semimajor axis, for triples with a WD in the inner binary. The shaded area represents the region where $a(1 - e_{\rm max})/a_{\rm Roche}$ 1. The outcome of the accretion depends on the components of the inner binary. WD–WD mergers can lead to Type Ia supernovae, while WD–NS and WD–BH mergers can lead to tidal disruption events and gamma-ray bursts (Hurley et al. 2002; Fryer et al. 1999; Perets et al. 2016; Fragione et al. 2019e).

We estimate that \sim 1.9%, 4.6%, and 4.2% of the systems merge for triples with inner WD–WD, WD–NS, and WD–BH binaries, respectively. We find that there is no significant difference between the case in which $T_{\rm enc}$ is computed using Equation (12) and the case in which $T_{\rm enc}$ goes to infinity (Hamers 2018), since for these systems the LK timescale is

typically smaller than the encounter timescale from Equation (12). Merging WDs have masses in the range of 0.2–1.4 M, while merging NSs and BHs have typical masses of ~1.3 and ~10 M, respectively. Assuming a GC density $\rho_{\rm GC}\sim 2.31\,{\rm Mpc}^{-3}$ (Rodriguez et al. 2015; Rodriguez & Loeb 2018), we estimate a merger rate ~10⁻³ Gpc⁻³ yr⁻¹, consistent with the estimated rate for this kind of merger in field triples (Fragione et al. 2019e).

5.3. Gravitational Wave Mergers in Triples with a Compact Object in the Inner Binary

For triples composed of an inner binary with two compact objects, GW emission becomes relevant. Given a binary of components M_1 and M_2 , semimajor axis a_{12} , and eccentricity e_{12} , it would merge through GW emission in isolation on a

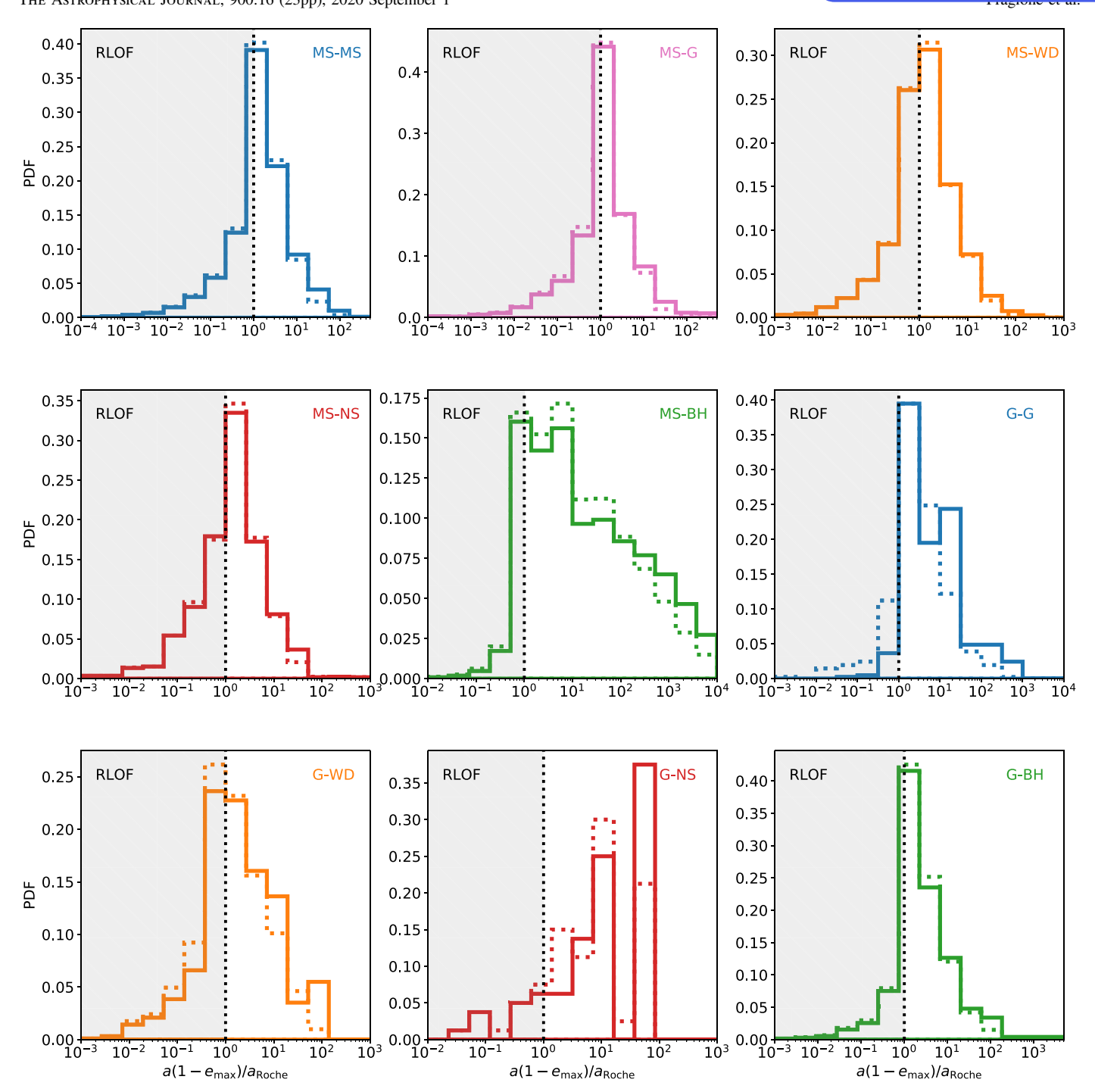


Figure 11. Probability distribution function of the ratio of the inner binary's pericenter during an LK cycle to the Roche semimajor axis (Equation (22)), for triples with an MS or a G star in the inner binary. The shaded area represents the region where a Roche lobe overflow can take place $(a(1 - e_{max})/a_{Roche})$ 1). Solid lines represent the condition $T_{LK} < T_{enc}$, and dotted lines represent the case in which T_{enc} goes to infinity.

timescale (Peters 1964)

$$T_{\rm GW} = \frac{5}{256} \frac{a_{12}^4 c^5}{G^3 (M_1 + M_2) M_1 M_2} (1 - e_{12}^2)^{7/2}.$$
 (24)

When LK oscillations are relevant in a triple system, the inner binary would spend a fraction of its time $\mu (1 - e_{\text{max}}^2)^{1/2}$ at $e \sim e_{\text{max}}$, where it loses energy efficiently owing to GW emission. Thus, the GW timescale would be reduced compared

to a binary in isolation (e.g., Grishin et al. 2018)

$$T_{\rm GW}^{\rm (red)} = \frac{5}{256} \frac{a_{12}^4 c^5}{G^3 (M_1 + M_2) M_1 M_2} (1 - e_{12}^2)^3.$$
 (25)

We show in Figure 13 the cumulative distribution function of the merger time ($T_{\rm f} + T_{\rm GW}^{\rm (red)}$) for triples with a WD in the inner binary. If the reduced GW merger time is shorter than the LK timescale that is required to reach the maximal eccentricity, we use the secular LK time (Fragione et al. 2019a). We find that \sim 0.6%, 2.5%, and 0.2% of the triples with inner WD–WD, WD–NS, and

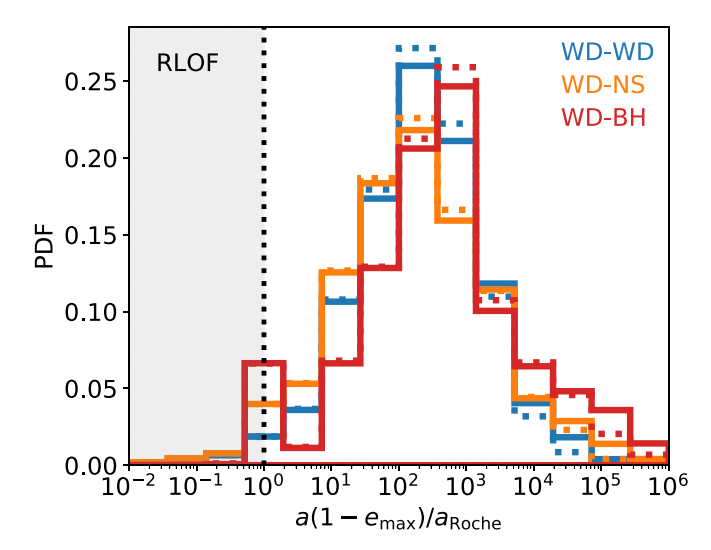


Figure 12. Probability distribution function of the ratio of the inner binary's pericenter during an LK cycle and the Roche semimajor axis, for triples with a WD in the inner binary. The shaded area represents the region where a Roche lobe overflow can take place $(a(1 - e_{\text{max}})/a_{\text{Roche}} - 1)$. Solid lines represent the condition $T_{\text{LK}} < T_{\text{enc}}$, and dotted lines represent the case in which T_{enc} goes to infinity.

WD-BH binaries merge owing to the LK mechanism within a Hubble time, respectively. We find no difference in the merger fractions when computing $T_{\rm enc}$ using Equation (12) and in the case in which $T_{\rm enc}$ goes to infinity, respectively.

Triples with an inner WD–BH and WD–NS binary could be observed by LISA up to the point of disruption. The GW frequency at disruption is 15 (Fragione et al. 2019e)

$$f_{\text{GW}} = \frac{G^{1/2} (M_2 + M_{\text{WD}})^{1/2}}{p R_{\text{t}}^{3/2}}$$

$$= 0.09 \text{ Hz} \left(1 + \frac{M_{\text{WD}}}{M_2} \right) M_{\text{WD}, 0.6 M}^{1/2} R_{\text{WD}, 10^4 \text{ km}}^{-3/2}, \quad (26)$$

where $R_{\rm WD} \mu M_{\rm WD}^{-1/3}$ is the WD radius and M_2 is the BH or NS mass. ¹⁶ The total characteristic GW strain for observing the GWs for a duration $T_{\rm obs}$ averaged over binary and detector orientation is approximately (Robson et al. 2019)

$$h_{\rm c} = \frac{8}{\sqrt{5}} \frac{G^2}{c^4} \frac{M_2 M_{\rm WD}}{R_t D} (T_{\rm obs} f_{\rm GW})^{1/2} = 2.0 \cdot 10^{-20}$$

$$T_{\rm obs,4yr}^{0.5} D_{10\,\rm Mpc}^{-1} M_{2,10\,\rm M}^{0.66} M_{\rm WD,0.6\,M}^{1.58} R_{\rm WD,10^4\,km}^{-1.75}. \tag{27}$$

In Figure 13, we also show the merging systems with an inner binary BH that merge owing to the LK mechanism. We estimate that $\sim 0.1\%$ of triples with a binary BH as inner binary merge within a Hubble time. We find that there is no significant difference between the cases in which the tertiary is any kind of object (BH–BH) or a BH (BH–BH–BH), thus implying that the majority of BH mergers due to the LK mechanism take place in triple systems where all the objects are BHs. Moreover, we find no difference in the merger fractions when computing $T_{\rm enc}$ using Equation (12) and in the case in which $T_{\rm enc}$ goes to infinity, respectively. None of the triples with an NS in the inner binary

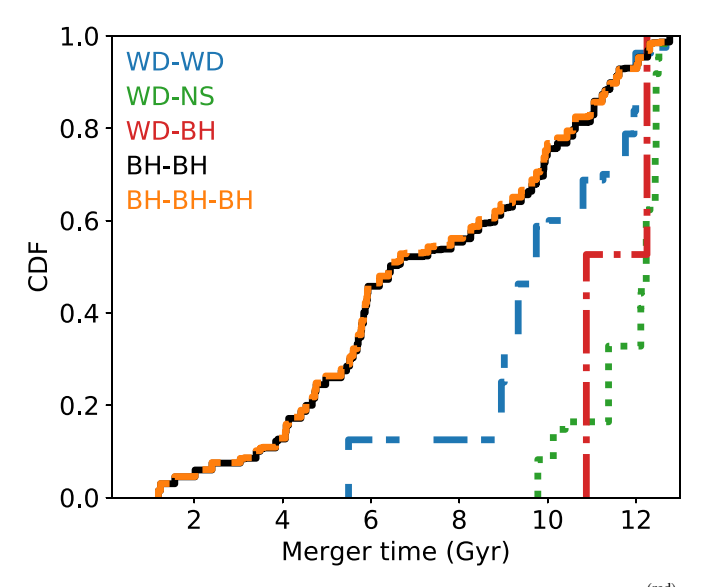


Figure 13. Cumulative distribution function of the merger time $(T_{\rm f} + T_{\rm GW}^{\rm fred})$, for triples with an inner binary composed of two compact objects that merge owing to the LK mechanism. The LK mechanism does not produce NS–NS or BH–NS mergers in our models.

merge within a Hubble time. The reason is that triples with NSs in the inner binary are formed at late times, when most of the BHs have been ejected in the BH-burning process (Kremer et al. 2019e), as shown in Figure 8. Therefore, triple systems likely do not contribute to the rates of NS–NS and BH–NS mergers in clusters, which remain too small to account for LIGO/Virgo observations, as shown in detail by Ye et al. (2020).

In order to estimate the local cosmological rate of BH-BH mergers in cluster triple systems, we compute the cumulative merger rate as (e.g., Rodriguez et al. 2015)

$$R(z) = \grave{\mathbf{Q}}^{z} \qquad (z \not \! \phi \frac{dV_c}{dz \not \! \phi} (1 + z \not \! \phi^{-1} dz \not \! \phi$$
 (28)

where dV_c/dz is the comoving volume at redshift z and (z) is the comoving (source) merger rate. The comoving rate is given by

$$(z) = f' r_{GC}' \frac{dN(z)}{dt}, \qquad (29)$$

where $\rho_{GC} \sim 2.31 \, \mathrm{Mpc}^{-3}$ (Rodriguez et al. 2015; Rodriguez & Loeb 2018), $f \sim 4$ is a scaling factor intended to incorporate the contribution of the cluster mass function's high-end tail not covered by our models (Kremer et al. 2020), and dN(z)/dt is the number of mergers per unit time at a given redshift. To estimate dN(z)/dt, we draw 10 random ages for the host cluster from the metallicity-dependent age distributions of El-Badry et al. (2018), where the merger originated, and then compute the effective merger time for each merger. We find that the merger rate for BH triples in star clusters is $\sim 0.1 \, \mathrm{Gpc}^{-3} \, \mathrm{yr}^{-1}$ in the local universe, consistent with Antonini et al. (2016), within the uncertainties. We leave a detailed calculation and discussion of the implications of BH mergers in triples to a companion paper (Martinez et al. 2020).

6. Discussion and Conclusions

Stellar multiplicity is an omnipresent outcome of the star formation process (Duchêne & Kraus 2013). More than \sim 50%

 $[\]overline{^{15}}$ Note that this corresponds to circular orbits, but the peak GW frequency at disruption is similar for arbitrary eccentricities to within $\sim\!\!20\%$.

We introduced the abbreviated notation $X_{,a} = X/a$.

and ${\sim}25\%$ of stars are thought to have at least one and two stellar companions, respectively. Hierarchical systems can also be formed in star clusters (Fregeau et al. 2004; Leigh & Geller 2013). In these dynamically active environments, fewbody interactions between stars and/or compact remnants can efficiently assemble hierarchical systems, primarily due to binary–binary encounters. In this process, one of the two binaries captures a star in the second wider binary, with the fourth object leaving the system.

In this paper, we have presented for the first time the demographics of triple systems of stars and compact objects assembled in dense star clusters of various masses, concentrations, and metallicities. We have made use of the ensemble of cluster simulations presented in Kremer et al. (2020), which covers roughly the complete range of GCs observed at present in the Milky Way.

We have demonstrated that triples are efficiently assembled in binary-binary encounters that involve two binaries of quite different sizes. In this process, the tighter binary replaces one of the components in the wider binary. The object that is removed is then ejected, while the captured one becomes the tertiary in the newly formed triple system. During these binary-binary encounters, triple formation can lead to GW captures and mergers of stars and compact objects. We have found that a cluster typically assembles hundreds of triples with an inner BH-BH binary (of which \sim 70%–90% have a BH as tertiary) or an inner MS-BH binary. Additionally, tens of triples with inner MS-MS and WD-BH binaries are produced. Only clusters with $r_{\rm v} \leq 1$ pc are efficient in assembling triples with inner binaries composed of MS-WD or WD-WD pairings. Due to the BH-burning process (Kremer et al. 2019e), these clusters produce ∼10 times more systems with inner MS–MS binaries. We have also found that $\sim 50\%$ of the overall triple population from our simulations consists of systems where all the components are BHs. Roughly 10% of the triples consist of an inner BH-BH binary with a non-BH tertiary companion, while \sim 38% consist of an inner binary containing at least one MS star. Other triples constitute the remaining $\sim 2\%$ of the population.

We have shown that the initial properties of the host cluster set the typical orbital parameters and formation times of the assembled triples. Smaller and less extended clusters form triples faster and with wider inner and outer orbits with respect to more massive and concentrated clusters. We have also found that triples whose inner binary comprises at least one BH typically form on a shorter timescale compared to other triples. This is a direct consequence of the BH-burning mechanism (Kremer et al. 2019e).

We have discussed how the LK mechanism can drive the inner binary of the formed triples to high eccentricities, whenever it takes place before the triple is dynamically reprocessed by encountering another cluster member. Some of these systems can reach sufficiently large eccentricities to form a variety of exotica, transients, and GW sources, such as blue stragglers, rejuvenated giant stars, X-ray binaries, Type Ia supernovae, Thorne–Zytkow objects, and LIGO/Virgo sources.

We have also estimated that the Milky Way's GCs are expected to host tens of triples with at least one luminous component at present. Due to their high densities, only one triple-star system is known to exist in GCs (e.g., Prodan & Murray 2012). The system in question, called 4U 1820-30, is located near the center of the GC NGC 6624 and consists of a low-mass X-ray binary with an NS

primary and a WD secondary, in orbit with a period of \sim 685 s. There is also a large luminosity variation for this system with a period of \sim 171 days, thought to be due to the presence of a tertiary companion (Grindlay et al. 1988). Another confirmed triple system in the GC M4 is made up of an inner binary composed of a pulsar (PSR 1620-26) and a WD, orbited by a substellar tertiary (Rasio et al. 1995; Arzoumanian et al. 1996). These systems could be naturally explained by binary-binary interactions involving planetary systems in dense stellar environments (Kremer et al. 2019b). A few nearby open clusters are also known to have comparably high multiplicity fractions (see, e.g., Leigh & Geller 2013, for a more detailed review). The Hyades (Patience et al. 1998), Pleiades (Mermilliod et al. 1992; Bouvier et al. 1997), and Praesepe (Mermilliod & Mayor 1999; Bouvier et al. 2001) have binary fractions of, respectively, 35%, 34%, and 40%, and triple fractions of, respectively, 6%, 3%, and 6%. Notably, the open cluster Taurus-Auriga appears to have a multiplicity fraction higher than the field. Kraus et al. (2011) performed a highresolution imaging study to characterize the multiple-star populations in Taurus-Auriga. They found that two-thirds to three-fourths of all targets are multiples composed of at least two stars. Therefore, only a quarter to a third of their objects are single stars.

Triple and hierarchical systems constitute a fundamental building block for many astrophysical phenomena, which are difficult to achieve with standard binary evolution (Naoz 2016). While current observations improve and provide unprecedented data on the galactic field population of triples, little is known on the triple population that can be assembled in dense star clusters. Upcoming instruments, such as LSST and JWST, may shed light on this population, which critically depends on the initial properties of the parent cluster and its evolutionary paths. In particular, a crucial role can be played by the primordial binary fraction and the mass ratio distributions of low- and high-mass stars. We leave to a future study further investigation of how triple formation and demographics depends on these parameters (G. Fragione et al. 2020, in preparation). While our current understanding of hierarchies in dense star clusters is still limited, the future of triple systems appears bright.

We are grateful to Nathan Leigh, Michael Shara, Rosanne di Stefano, and Selma de Mink for useful discussions. Our work was supported by NSF grant AST-1716762. Computations were supported in part through the resources and staff contributions provided for the Quest high-performance computing facility at Northwestern University, which is jointly supported by the Office of the Provost, the Office for Research, and Northwestern University Information Technology. This work also used computing resources at CIERA funded by NSF grant PHY-1726951 and computing resources provided by Northwestern University and the Center for Interdisciplinary Exploration and Research in Astrophysics (CIERA). G.F. acknowledges support from a CIERA postdoctoral fellowship at Northwestern University. S.C. acknowledges support from the Department of Atomic Energy, Government of India, under project No. 12-R&D-TFR-5.02-0200. S.N. acknowledges the partial support of NASA grant Nos. 80NSSC19K0321 and 80NSSC20K0505 and also thanks Howard and Astrid Preston for their generous support.

Appendix Triple Systems Formed in Cluster Simulations

We include in the Appendix two tables (Tables A1 and A2) containing more detailed information for each simulation.



 Table A1

 Initial Cluster Parameters and Number of Different Triples Formed

	r _v (pc)	rg (kpc)	Z	N	MS-MS	MS-G	MS-WD	MS-NS	MS-BH	G–G	G–WD	G–NS	G–BH
1	0.5	2	0.0002	2×10^{5}	150	16	17	0	314	0	0	0	6
2	0.5	2	0.0002	4×10^{5}	326	12	67	0	1192	1	1	0	6
3 4 [†]	0.5	2	0.0002	8×10^5	180	1	33	13	312	0	0	0	4
4	0.5	2	0.0002	1.6×10^{6}	24	0	0	0	0	0	0	0	0
5	0.5	2	0.002	2×10^{5}	314	21	21	1	553	0	2	0	0
6	0.5	2	0.002	4×10^{5} 8×10^{5}	261	6	78	6	330	0	2	0	5
7 8	0.5 0.5	2 2	0.002 0.002	1.6×10^{6}	251 201	7 3	66 2	7 0	259 154	0	1 0	2	0
9 10	0.5 0.5	2 2	0.02 0.02	2×10^{5} 4×10^{5}	283 298	37 23	10 50	4 5	40 51	14 3	1 10	0	1 0
11	0.5	2	0.02	8×10^5	342	16	51	9	101	0	0	1	8
12	0.5	2	0.02	1.6×10^6	412	10	81	10	109	0	0	0	2
13	0.5	8	0.0002	2×10^{5}	281	44	44	2	664	3	2	0	16
14	0.5	8	0.0002	4×10^5	248	2	37	4	866	0	3	0	5
15	0.5	8	0.0002	8×10^5	184	1	41	6	258	0	1	0	1
16 [†]	0.5	8	0.0002	1.6×10^{6}	35	0	0	0	0	0	0	0	0
17	0.5	8	0.002	2×10^5	293	10	66	6	358	0	1	0	5
18	0.5	8	0.002	4×10^{5}	247	4	53	5	350	0	0	0	2
19	0.5	8	0.002	8×10^{5}	237	7	34	8	230	0	0	0	1
20	0.5	8	0.002	1.6×10^{6}	190	1	1	0	97	0	0	0	1
21	0.5	8	0.02	2×10^{5}	221	21	38	1	134	3	1	0	3
22	0.5	8	0.02	4×10^5	279	17	38	2	100	0	7	3	9
23 24	0.5 0.5	8 8	0.02 0.02	8×10^5 1.6×10^6	283 349	10 7	53 60	3 4	122 142	0	2 2	0	2 6
25	0.5	20	0.0002	2×10^{5} 4×10^{5}	232	6	70	1	600	0	1	0	1
26 27	0.5 0.5	20 20	0.0002 0.0002	4×10^{5} 8×10^{5}	294 168	2 3	21 39	3 8	623 308	0	0	0	3 1
28 [†]	0.5	20	0.0002	1.6×10^{6}	38	0	0	0	0	0	0	0	0
29	0.5	20	0.002	2×10^{5}	298	17	86	3	463	4	5	0	3
30	0.5	20	0.002	4×10^5	272	6	44	2	551	0	2	0	1
31	0.5	20	0.002	8×10^{5}	187	3	29	1	180	0	1	0	0
32	0.5	20	0.002	1.6×10^{6}	132	5	1	0	160	0	0	0	0
33	0.5	20	0.02	2×10^5	301	25	38	2	84	1	3	0	2
34	0.5	20	0.02	4×10^{5}	277	5	24	2	59	0	0	0	6
35	0.5	20	0.02	8×10^5	291 360	13	46	5	100	0	3	0	3
36	0.5	20	0.02	1.6×10^{6}		8	62	8	103	0	3	0	2
37	1	2	0.0002	2×10^{5}	70	2	38	2	259	0	1	0	4
38	1	2	0.0002	$4 \times 10^5 \\ 8 \times 10^5$	81	1	61	3	209	0	3	0	1
39 40	1 1	2 2	0.0002 0.0002	1.6×10^{6}	17 21	1 0	2	0	159 85	0	0	0	0 1
41 42	1 1	2 2	0.002 0.002	$\begin{array}{c} 2 \times 10^5 \\ 4 \times 10^5 \end{array}$	85 92	1 4	34 57	0 2	252 370	0	3 2	0	3
43	1	2	0.002	8×10^{5}	17	0	0	0	227	0	0	0	0
44	1	2	0.002	1.6×10^{6}	8	0	0	0	87	0	0	0	0
45	1	2	0.02	2×10^{5}	127	11	34	1	32	5	4	0	9
46	1	2	0.02	4×10^5	157	3	36	1	105	0	4	1	11
47	1	2	0.02	8×10^5	182	15	44	1	62	0	2	0	3
48	1	2	0.02	1.6×10^{6}	97	4	6	0	107	0	0	0	3
49	1	8	0.0002	2×10^{5}	97	2	48	1	528	0	2	0	1
50	1	8	0.0002	4×10^5	50	0	35	5	332	0	0	0	0
51	1	8	0.0002	8×10^{5}	15	0	0	0	150	0	0	0	0
52	1	8	0.0002	1.6×10^{6}	17	2	1	0	88	0	0	0	0
53	1	8	0.002	2×10^{5}	119	4	41	0	396	0	1	0	2
54	1	8	0.002	4×10^5	30	1	2	0	163	0	1	0	1
55 56	1 1	8 8	0.002 0.002	8×10^5 1.6×10^6	17 15	0	0 1	0	137 141	0	0	0	0
50	1	o	0.002	1.0 \ 10	13	U	1	U	1+1	U	U	U	U

Table A1 (Continued)

						(Cont	illueu)						
	$r_{\rm v}$ (pc)	$r_{\rm g}$ (kpc)	Z	N	MS-MS	MS-G	MS-WD	MS-NS	MS-BH	G–G	G-WD	G-NS	G–BH
57	1	8	0.02	2×10^{5}	142	16	45	0	76	3	2	0	8
58	1	8	0.02	4×10^{5}	158	18	46	1	63	0	2	0	4
59	1	8	0.02	8×10^{5}	159	11	20	0	65	0	1	0	3
60	1	8	0.02	1.6×10^{6}	88	3	2	0	78	0	0	0	3
61	1	20	0.0002	2×10^{5}	72	2	53	3	309	0	1	0	1
62	1	20	0.0002	4×10^{5}	82	2	59	9	532	0	0	0	2
63	1	20	0.0002	8×10^{5}	15	1	0	0	135	0	0	0	0
64	1	20	0.0002	1.6×10^{6}	10	0	0	0	130	0	0	0	0
65	1	20	0.002	2×10^{5}	104	7	30	0	566	0	1	0	3
66	1	20	0.002	4×10^{5}	51	1	12	1	331	0	0	0	4
67	1	20	0.002	8×10^5	14	0	1	0	294	0	0	0	1
68	1	20	0.002	1.6×10^{6}	12	1	0	0	91	0	0	0	0
69	1	20	0.02	2×10^{5}	120	29	57	0	90	2	3	0	2
70	1	20	0.02	4×10^{5}	123	5	29	1	99	0	0	0	11
71	1	20	0.02	8×10^5	120	7	10	1	86	0	0	1	2
72	1	20	0.02	1.6×10^{6}	89	0	2	0	40	0	0	0	0
73	2	2	0.0002	2×10^{5}	46	1	15	0	559	0	0	0	2
74	2	2	0.0002	4×10^{5}	34	0	20	0	269	0	0	0	1
75 76	2	2	0.0002	8×10^5	9	0	0	0	143	0	0	0	0
76	2	2	0.0002	1.6×10^{6}	7	0	0	0	67	0	0	0	0
77	2	2	0.002	2×10^{5}	34	3	16	0	218	0	1	0	0
78	2	2	0.002	4×10^{5}	34	1	13	0	292	0	0	0	0
79	2	2	0.002	8×10^5	8	0	1	0	224	0	0	0	0
80	2	2	0.002	1.6×10^{6}	8	0	0	0	72	0	0	0	2
81	2	2	0.02	2×10^{5}	35	8	4	0	29	0	0	0	2
82	2	2	0.02	4×10^{5}	34	5	9	0	26	0	0	0	1
83	2	2	0.02	8×10^{5}	30	0	0	0	18	0	0	0	3
84	2	2	0.02	1.6×10^{6}	37	0	0	0	21	0	0	0	0
85	2	8	0.0002	2×10^{5}	2	0	6	0	300	0	0	0	0
86	2	8	0.0002	4×10^{5}	9	0	2	0	226	0	0	0	0
87	2	8 8	0.0002	8×10^5	8	0	0	0	65	0	0	0	1
88	2		0.0002	1.6×10^{6}	8	0	-	0	46	0	0	0	0
89	2	8	0.002	2×10^{5}	64	6	48	0	390	0	3	0	4
90	2	8	0.002	4×10^{5}	8	0	0	0	307	0	0	0	0
91	2	8 8	0.002	8×10^5 1.6×10^6	7 5	0	0	0	105	0	0	0	0
92	2		0.002		3	0	0		81		0	0	
93	2	8	0.02	2×10^{5}	27	0	4	0	20	0	0	0	1
94	2	8	0.02	4×10^{5}	23	0	5	0	20	0	0	0	2
95 96	2 2	8 8	0.02 0.02	8×10^5 1.6×10^6	16 35	1 1	1 0	0	26 20	1 0	0	0	2
97	2	20	0.0002	2×10^{5}	14	0	6	0	324	0	0	0	1
98	2	20	0.0002	4×10^{5}	15	0	2	1	212	0	0	0	0
99 100	2 2	20 20	0.0002 0.0002	8×10^5 1.6×10^6	2 9	0	0	0	124 47	0	0	0	3
101	2	20	0.002	2×10^{5}	16	0	0	0	231	0	0	0	0
102	2	20	0.002	4×10^{5} 8×10^{5}	11	0	1	0	186	0	0	0	0
103 104	2 2	20 20	0.002 0.002	8×10^{6} 1.6×10^{6}	2 10	0 1	1 0	0	126 70	0	0	0	0 1
105	2	20	0.02	2×10^5	29	4	5	0	16	0	0	0	0
106	2	20	0.02	4×10^{5} 8×10^{5}	23	1	0	0	37	0	0	0	1
107 108	2 2	20 20	0.02 0.02	8×10^{6} 1.6×10^{6}	19 26	0 1	1 0	0	20 75	0 1	0	0	2 0
109	4	2	0.0002	2×10^{5}	1	0	0	0	236	0	0	0	0
110	4	2 2	0.0002 0.0002	4×10^{5} 8×10^{5}	1	0	0	0	167 60	0	0	0	0
111 112	4 4	2	0.0002	8×10^{6} 1.6×10^{6}	2 5	0	0	0	265	0	0	0	0
112			0.0002	1.0 \ 10	J	0	0		203	0	0	U	

Table A1 (Continued)

						(Cont	mucu)						
	r _v (pc)	r _g (kpc)	Z	N	MS-MS	MS-G	MS-WD	MS-NS	MS-BH	G–G	G–WD	G-NS	G–BH
113	4	2	0.002	2×10^{5}	1	1	0	0	265	0	0	0	0
114	4	2	0.002	4×10^5	3	0	0	0	198	0	0	0	0
115	4	2	0.002	8×10^{5}	0	0	0	0	167	0	0	0	0
116	4	2	0.002	1.6×10^{6}	4	0	0	0	104	0	0	0	0
117	4	2	0.02	2×10^{5}	1	0	0	0	3	0	0	0	0
118	4	2	0.02	4×10^{5}	5	0	2	0	11	0	0	0	1
119	4	2	0.02	8×10^{5}	11	0	0	0	11	0	0	0	1
120	4	2	0.02	1.6×10^{6}	17	0	2	0	10	0	0	0	0
121	4	8	0.0002	2×10^5	4	0	0	0	554	0	0	0	7
122	4	8	0.0002	4×10^{5}	2	0	0	0	205	0	0	0	0
123	4	8	0.0002	8×10^{5}	2	0	0	0	64	0	0	0	0
124	4	8	0.0002	1.6×10^6	2	0	0	0	36	0	0	0	0
125	4	8	0.002	2×10^{5}	4	0	1	0	280	0	0	0	0
126	4	8	0.002	4×10^5	6	0	1	0	211	0	0	0	0
127	4	8	0.002	8×10^5	3	0	0	0	178	0	0	0	0
128	4	8	0.002	1.6×10^{6}	6	0	0	0	125	0	0	0	0
129	4	8	0.02	2×10^{5}	7	0	2	0	13	0	0	0	0
130	4	8	0.02	4×10^5	7	0	7	0	10	0	0	0	0
131	4	8	0.02	8×10^5	7	0	2	0	11	0	0	0	1
132	4	8	0.02	1.6×10^{6}	14	1	0	0	10	0	0	0	2
133	4	20	0.0002	2×10^5	1	0	0	0	231	0	0	0	0
134	4	20	0.0002	4×10^5	2	0	2	0	168	0	0	0	2
135	4	20	0.0002	8×10^{5}	2	0	0	0	83	0	0	0	0
136	4	20	0.0002	1.6×10^{6}	6	0	0	0	34	0	0	0	0
137	4	20	0.002	2×10^{5}	6	1	2	0	250	0	0	0	1
138	4	20	0.002	4×10^5	4	0	0	0	268	0	0	0	1
139	4	20	0.002	8×10^5	4	0	0	0	175	0	0	0	0
140	4	20	0.002	1.6×10^{6}	4	0	0	0	59	0	0	0	0
141	4	20	0.02	2×10^{5}	5	0	1	0	10	0	0	0	1
142	4	20	0.02	4×10^{5}	10	0	0	0	5	0	0	0	0
143	4	20	0.02	8×10^{5}	10	1	1	0	6	0	0	0	0
144	4	20	0.02	1.6×10^{6}	13	0	1	0	8	0	0	0	0
145	1	20	0.0002	3.2×10^{6}	14	0	0	0	26	0	0	0	0
146	2	20	0.0002	3.2×10^{6}	11	0	0	0	37	0	0	0	0
147	1	20	0.02	3.2×10^{6}	49	0	0	0	29	0	0	0	0
148	2	20	0.02	3.2×10^{6}	44	1	3	0	31	0	0	0	1

Note. Triples with an MS star or a giant plus a companion in the inner binary. Models marked with a dagger (†) indicate that the model was stopped owing to onset of collisional runaway (see Kremer et al. 2020, for details).

Table A2
Initial Cluster Parameters and Number of Different Triples Formed

	r _v (pc)	r _g (kpc)	Z	N	WD-WD	WD-NS	WD-BH	NS-NS	NS-BH	BH–BH	BH-BH-BH
1	0.5	2	0.0002	2×10^{5}	2	0	11	0	0	265	170
2	0.5	2	0.0002	4×10^{5}	18	11	3	0	0	562	301
3	0.5	2	0.0002	8×10^{5}	42	16	27	4	0	755	635
4^{\dagger}	0.5	2	0.0002	1.6×10^{6}	0	0	0	0	0	0	0
5	0.5	2	0.002	2×10^{5}	6	0	7	0	0	263	232
6	0.5	2	0.002	4×10^{5}	50	3	10	0	1	422	369
7	0.5	2	0.002	8×10^{5}	30	15	8	1	0	662	610
8	0.5	2	0.002	1.6×10^{6}	0	0	3	0	0	973	949
9	0.5	2	0.02	2×10^{5}	1	0	0	0	0	188	152
10	0.5	2	0.02	4×10^{5}	25	8	1	0	0	263	234
11	0.5	2	0.02	8×10^{5}	18	11	8	0	1	291	271
12	0.5	2	0.02	1.6×10^{6}	18	4	17	1	0	438	412

Table A2 (Continued)

						Continued)					
	$r_{\rm v}~({\rm pc})$	$r_{\rm g}~({\rm kpc})$	Z	N	WD-WD	WD-NS	WD-BH	NS-NS	NS-BH	ВН–ВН	ВН–ВН–ВН
13	0.5	8	0.0002	2×10^{5}	20	12	5	0	2	246	125
14	0.5	8	0.0002	4×10^{5}	125	31	75	3	0	692	467
15	0.5	8	0.0002	8×10^{5}	34	24	16	3	6	797	694
16 [†]	0.5	8	0.0002	1.6×10^{6}	0	0	0	0	0	0	0
17	0.5	8	0.002	2×10^{5}	41	1	1	0	0	267	236
18	0.5	8	0.002 0.002	4×10^5 8×10^5	16	0	9	0	0	479	438
19	0.5	8		8×10^6 1.6×10^6	24 0	4	12 0	2	0	555	521
20	0.5	8	0.002		-	0			-	898	867
21 22	0.5 0.5	8 8	0.02 0.02	$\begin{array}{c} 2 \times 10^5 \\ 4 \times 10^5 \end{array}$	54 23	3 1	3 20	0	0	82 150	72 141
23	0.5	8	0.02	8×10^{5}	11	4	41	0	2	328	278
24	0.5	8	0.02	1.6×10^{6}	8	5	11	1	3	473	446
25	0.5	20	0.0002	2×10^{5}	39	5	1	2	0	303	181
26	0.5	20	0.0002 0.0002	4×10^{5} 8×10^{5}	5	1	39	0	5	600	425
27 28 [†]	0.5 0.5	20 20	0.0002	1.6×10^6	33 0	18 0	5 0	1 0	4 0	877 0	733 0
				$\frac{2\times10^5}{}$							
29 30	0.5 0.5	20 20	0.002 0.002	4×10^{5}	38 29	7	39 15	0	0	269 445	213 378
31	0.5	20	0.002	4×10^{5} 8×10^{5}	13	1 5	19	0	0	739	682
32	0.5	20	0.002	1.6×10^{6}	0	0	0	0	0	1034	999
					-						
33	0.5	20	0.02	2×10^{5}	7	0	10	0	0	157	143
34	0.5	20	0.02	4×10^{5}	8	1	4	0	0	218	203
35	0.5	20	0.02	8×10^5	6	5	16	0	10	345	330
36	0.5	20	0.02	1.6×10^{6}	11	2	13	0	0	516	480
37	1	2	0.0002	2×10^{5}	18	0	59	0	0	446	290
38	1	2	0.0002	4×10^{5}	67	10	5	1	1	628	485
39	1	2	0.0002	8×10^5	0	0	0	0	0	907	785
40	1	2	0.0002	1.6×10^{6}	0	0	2	0	0	1038	981
41	1	2	0.002	2×10^{5}	28	0	14	0	1	285	231
42	1	2	0.002	4×10^{5}	56	2	41	0	0	620	517
43	1	2	0.002	8×10^{5}	0	0	4	0	0	704	629
44	1	2	0.002	1.6×10^6	0	0	0	0	0	807	753
45	1	2	0.02	2×10^{5}	2	0	0	0	0	132	119
46	1	2	0.02	4×10^{5}	7	1	38	0	5	230	216
47	1	2	0.02	8×10^{5}	13	2	10	0	0	308	294
48	1	2	0.02	1.6×10^{6}	0	0	7	0	0	559	537
49	1	8	0.0002	2×10^{5}	33	3	6	0	0	486	284
50	1	8	0.0002	4×10^{5}	38	4	24	0	1	738	582
51	1	8	0.0002	8×10^{5}	0	0	1	0	0	789	712
52	1	8	0.0002	1.6×10^{6}	0	0	0	0	0	978	906
53	1	8	0.002	2×10^{5}	22	0	42	0	0	329	275
54	1	8	0.002	4×10^{5}	1	0	2	0	0	571	491
55	1	8	0.002	8×10^{5}	0	0	3	0	0	879	793
56	1	8	0.002	1.6×10^{6}	0	0	0	0	0	962	916
57	1	8	0.02	2×10^{5}	7	0	1	0	0	210	196
58	1	8	0.02	4×10^{5}	13	3	2	0	0	325	315
59	1	8	0.02	8×10^{5}	3	1	24	0	0	411	394
60	1	8	0.02	1.6×10^{6}	0	0	7	0	0	486	471
61	1	20	0.0002	2×10^{5}	46	3	5	0	2	421	276
62	1	20	0.0002	4×10^{5}	40	11	15	1	2	809	523
63	1	20	0.0002	8×10^{5}	0	0	5	0	0	963	856
64	1	20	0.0002	1.6×10^{6}	0	0	1	0	0	893	849
65	1	20	0.002	2×10^{5}	14	0	26	0	0	415	352
66	1	20	0.002	4×10^{5}	4	1	4	0	0	634	516
67	1	20	0.002	8×10^5	0	0	1	0	0	745	671
68	1	20	0.002	1.6×10^{6}	0	0	0	0	0	1016	960

Table A2 (Continued)

					(Continued)					
	$r_{\rm v}$ (pc)	r _g (kpc)	Z	N	WD-WD	WD-NS	WD-BH	NS-NS	NS-BH	BH–BH	BH-BH-BH
69	1	20	0.02	2×10^{5}	10	0	1	0	0	178	163
70	1	20	0.02	4×10^{5}	8	1	9	0	0	300	282
71	1	20	0.02	8×10^{5}	3	0	4	0	0	399	383
72	1	20	0.02	1.6×10^{6}	0	0	5	0	0	484	474
73	2	2	0.0002	2×10^{5}	4	0	33	0	0	415	227
74	2	2	0.0002	4×10^{5}	25	3	9	0	0	755	571
75 75	2	2	0.0002	8×10^{5}	0	0	0	0	0	908	734
76	2	2	0.0002	1.6×10^{6}	0	0	0	0	0	1055	960
77	2	2	0.002	2×10^{5}	3	0	5	0	0	472	333
78	2	2	0.002	4×10^{5}	3	0	7	0	1	731	551
79	2	2	0.002	8×10^5	0	0	0	0	0	786	650
80	2	2	0.002	1.6×10^{6}	0	0	1	0	0	855	765
81	2	2	0.02	2×10^{5}	0	0	1	0	0	231	218
82	2	2	0.02	4×10^{5}	2	0	2	0	0	245	238
83	2	2	0.02	8×10^5	0	0	2	0	0	347	346
84	2	2	0.02	1.6×10^{6}	0	0	0	0	0	450	446
85	2	8	0.0002	2×10^{5}	2	0	2	0	0	410	257
86	2	8	0.0002	4×10^{5}	0	0	0	0	0	688	488
87	2	8	0.0002	8×10^{5}	0	0	2	0	0	783	640
88	2	8	0.0002	1.6×10^{6}	0	0	0	0	0	779	715
89	2	8	0.002	2×10^{5}	18	0	3	0	0	398	268
90	2	8	0.002	4×10^{5}	0	0	3	0	0	748	600
91	2	8	0.002	8×10^{5}	0	0	0	0	0	725	583
92	2	8	0.002	1.6×10^{6}	0	0	0	0	0	810	706
93	2	8	0.02	2×10^5	0	0	0	0	0	160	145
94	2	8	0.02	4×10^{5}	0	0	0	0	0	288	282
95	2	8	0.02	8×10^{5}	0	0	0	0	0	367	359
96	2	8	0.02	1.6×10^{6}	0	0	0	0	0	437	434
97	2	20	0.0002	2×10^5	2	0	5	0	1	510	306
98	2	20	0.0002	4×10^5	0	0	3	0	0	690	504
99	2	20	0.0002	8×10^{5}	0	0	1	0	0	817	686
100	2	20	0.0002	1.6×10^{6}	0	0	7	0	0	857	796
101	2	20	0.002	2×10^5	0	0	4	0	0	337	222
102	2	20	0.002	4×10^5	0	0	1	0	0	634	481
103	2	20	0.002	8×10^{5}	0	0	2	0	0	755	616
104	2	20	0.002	1.6×10^{6}	0	0	0	0	0	931	822
105	2	20	0.02	2×10^5	0	0	2	0	0	195	186
106	2	20	0.02	4×10^{5}	0	0	0	0	0	263	257
107	2	20	0.02	8×10^{5}	0	0	1	0	0	295	293
108	2	20	0.02	1.6×10^{6}	0	0	5	0	0	443	437
109	4	2	0.0002	2×10^{5}	0	0	0	0	0	211	107
110	4	2	0.0002	4×10^{5}	0	0	9	0	0	399	268
111	4	2	0.0002	8×10^{5}	0	0	0	0	0	469	328
112	4	2	0.0002	1.6×10^{6}	0	0	0	0	0	797	710
113	4	2	0.002	2×10^{5}	0	0	1	0	0	101	37
114	4	2	0.002	4×10^{5}	0	0	2	0	0	358	241
115	4	2	0.002	8×10^{5}	0	0	0	0	0	555	392
116	4	2	0.002	1.6×10^{6}	0	0	0	0	0	722	597
117	4	2	0.02	2×10^{5}	0	0	0	0	0	103	100
118	4	2	0.02	4×10^5	0	0	0	0	0	229	225
119	4	2	0.02	8×10^{5}	0	0	0	0	0	288	283
120	4	2	0.02	1.6×10^{6}	0	0	0	0	0	333	330
121	4	8	0.0002	2×10^{5}	1	0	23	0	0	376	170
122	4	8	0.0002	4×10^{5}	0	0	2	0	0	629	425
123	4	8	0.0002	8×10^{5}	0	0	5	0	0	664	543
124	4	8	0.0002	1.6×10^{6}	0	0	0	0	0	558	487

Table A2 (Continued)

	$r_{\rm v}$ (pc)	$r_{\rm g}~({\rm kpc})$	Z	N	WD-WD	WD-NS	WD-BH	NS-NS	NS-BH	BH–BH	ВН–ВН–ВН
125	4	8	0.002	2×10^{5}	0	0	4	0	0	381	225
126	4	8	0.002	4×10^{5}	0	0	0	0	0	567	434
127	4	8	0.002	8×10^{5}	0	0	0	0	0	817	622
128	4	8	0.002	1.6×10^{6}	0	0	1	0	0	876	728
129	4	8	0.02	2×10^{5}	0	0	0	0	0	157	149
130	4	8	0.02	4×10^{5}	0	0	0	0	0	226	223
131	4	8	0.02	8×10^{5}	0	0	0	0	0	206	204
132	4	8	0.02	1.6×10^{6}	0	0	0	0	0	321	318
133	4	20	0.0002	2×10^{5}	0	0	12	0	0	432	254
134	4	20	0.0002	4×10^{5}	0	0	7	0	0	613	411
135	4	20	0.0002	8×10^{5}	0	0	0	0	0	640	498
136	4	20	0.0002	1.6×10^{6}	0	0	0	0	0	648	549
137	4	20	0.002	2×10^{5}	0	0	3	0	0	348	206
138	4	20	0.002	4×10^5	0	0	5	0	0	574	409
139	4	20	0.002	8×10^{5}	0	0	2	0	0	712	517
140	4	20	0.002	1.6×10^{6}	0	0	0	0	0	614	512
141	4	20	0.02	2×10^{5}	0	0	1	0	0	146	139
142	4	20	0.02	4×10^{5}	0	0	0	0	0	153	152
143	4	20	0.02	8×10^{5}	0	0	0	0	0	230	227
144	4	20	0.02	1.6×10^{6}	0	0	1	0	0	338	337
145	1	20	0.0002	3.2×10^{6}	0	0	0	0	0	509	491
146	2	20	0.0002	3.2×10^{6}	0	0	0	0	0	687	667
147	1	20	0.02	3.2×10^{6}	0	0	0	0	0	417	408
148	2	20	0.02	3.2×10^{6}	0	0	0	0	0	496	490

Note. Triples with a WD, NS, or BH plus a companion in the inner binary. Models marked with a dagger (†) indicate that the model was stopped owing to onset of collisional runaway (see Kremer et al. 2020, for details).

ORCID iDs

Giacomo Fragione https://orcid.org/0000-0002-7330-027X Miguel A. S. Martinez https://orcid.org/0000-0001-5285-4735

Kyle Kremer https://orcid.org/0000-0002-4086-3180 Sourav Chatterjee https://orcid.org/0000-0002-3680-2684 Carl L. Rodriguez https://orcid.org/0000-0003-4175-8881 Claire S. Ye https://orcid.org/0000-0001-9582-881X Newlin C. Weatherford https://orcid.org/0000-0002-9660-9085

Smadar Naoz https://orcid.org/0000-0002-9802-9279 Frederic A. Rasio https://orcid.org/0000-0002-7132-418X

References

Aarseth, S. J., & Heggie, D. C. 1976, A&A, 53, 259
Anderson, K. R., Lai, D., & Storch, N. I. 2017, MNRAS, 467, 3066
Anderson, K. R., Storch, N. I., & Lai, D. 2016, MNRAS, 456, 3671
Antognini, J. M. O., & Thompson, T. A. 2016, MNRAS, 456, 4219
Antonini, F., Chatterjee, S., Rodriguez, C. L., et al. 2016, ApJ, 816, 65
Arzoumanian, Z., Joshi, K., Rasio, F. A., & Thorsett, S. E. 1996, in ASP Conf. Ser. 105, IAU Coll. 160: Pulsars: Problems and Progress, ed. S. Johnston, M. A. Walker, & M. Bailes (San Francisco, CA: ASP), 525
Askar, A., Szkudlarek, M., Gondek-Rosińska, D., Giersz, M., & Bulik, T. 2017, MNRAS, 464, L36
Banerjee, S. 2017, MNRAS, 467, 524
Banerjee, S., Baumgardt, H., & Kroupa, P. 2010, MNRAS, 402, 371
Baumgardt, H., & Hilker, M. 2018, MNRAS, 478, 1520
Belczynski, K., Heger, A., Gladysz, W., et al. 2016, A&A, 594, A97
Belczynski, K., Kalogera, V., & Bulik, T. 2002, ApJ, 572, 407

Binney, J., & Tremaine, S. 2008, Galactic Dynamics: Second Edition

(Princeton, NJ: Princeton Univ. Press)

Bouvier, J., Duchêne, G., Mermilliod, J.-C., & Simon, T. 2001, A&A, 375, 989 Bouvier, J., Rigaut, F., & Nadeau, D. 1997, A&A, 323, 139 Chatterjee, S., Fregeau, J. M., Umbreit, S., & Rasio, F. A. 2010, ApJ, 719, 915 Chatterjee, S., Rodriguez, C. L., Kalogera, V., & Rasio, F. A. 2017a, ApJL, 836, L26 Chatterjee, S., Rodriguez, C. L., & Rasio, F. A. 2017b, ApJ, 834, 68 Chatterjee, S., Umbreit, S., Fregeau, J. M., & Rasio, F. A. 2013, MNRAS, 429, 2881 Chen, X., Madau, P., Sesana, A., & Liu, F. K. 2009, ApJL, 697, L149 Chini, R., Hoffmeister, V. H., Nasseri, A., Stahl, O., & Zinnecker, H. 2012, S, 424, 1925 Clark, G. 1975, ApJL, 199, L143 Dehnen, W., & Binney, J. 1998, MNRAS, 294, 429 Duchêne, G., & Kraus, A. 2013, ARA&A, 51, 269 Duquennoy, A., & Mayor, M. 1991, A&A, 500, 337 Eggleton, P. P. 1983, ApJ, 268, 368 Eggleton, P. P., & Kiseleva-Eggleton, L. 2001, ApJ, 562, 1012 El-Badry, K., Quataert, E., Weisz, D. R., Choksi, N., & Boylan-Kolchin, M. 2018, arXiv:1805.03652 Fabrycky, D., & Tremaine, S. 2007, ApJ, 669, 1298 Ford, E. B., Kozinsky, B., & Rasio, F. A. 2000, ApJ, 535, 385 Fragione, G., Grishin, E., Leigh, N. W. C., Perets, H. B., & Perna, R. 2019a, NRAS, 488, 47 Fragione, G., & Kocsis, B. 2018, PhRvL, 121, 161103 Fragione, G., & Kocsis, B. 2019, MNRAS, 486, 4781 Fragione, G., & Kocsis, B. 2020, MNRAS, 493, 3920 Fragione, G., & Leigh, N. 2018, MNRAS, 479, 3181 Fragione, G., Leigh, N. W. C., & Perna, R. 2019b, MNRAS, 488, 2825 Fragione, G., Leigh, N. W. C., Perna, R., & Kocsis, B. 2019c, MNRAS, 489, 727 Fragione, G., Loeb, A., & Ginsburg, I. 2019d, MNRAS, 483, 648 Fragione, G., Metzger, B. D., Perna, R., Leigh, N. W. C., & Kocsis, B. 2019e, arXiv:1908.00987

Fragione, G., Pavlík, V., & Banerjee, S. 2018, MNRAS, 480, 4955

Fregeau, J. M., Cheung, P., Portegies Zwart, S. F., & Rasio, F. A. 2004,

MNRAS, 352, 1

```
Fregeau, J. M., Gurkan, M. A., Joshi, K. J., & Rasio, F. A. 2003, ApJ, 593, 772
Fregeau, J. M., & Rasio, F. A. 2007, ApJ, 658, 1047
Fryer, C. L., Belczynski, K., Wiktorowicz, G., et al. 2012, ApJ, 749, 91
Fryer, C. L., & Kalogera, V. 2001, ApJ, 554, 548
Fryer, C. L., Woosley, S. E., Herant, M., & Davies, M. B. 1999, ApJ, 520, 650
Giesler, M., Clausen, D., & Ott, C. D. 2018, MNRAS, 477, 1853
Grindlay, J. E., Bailyn, C. D., Cohn, H., et al. 1988, ApJL, 334, L25
Grishin, E., Perets, H. B., & Fragione, G. 2018, MNRAS, 481, 4907
Hamers, A. S. 2018, MNRAS, 476, 4139
Hamers, A. S., Bar-Or, B., Petrovich, C., & Antonini, F. 2018, ApJ, 865, 2
Harris, W. E. 1996, AJ, 112, 1487
Heggie, D., & Hut, P. 2003, The Gravitational Million-Body Problem: A
   Multidisciplinary Approach to Star Cluster Dynamics (Cambridge:
   Cambridge Univ. Press), 372
Heggie, D. C. 1975, MNRAS, 173, 729
Heinke, C. O., Grindlay, J. E., Edmonds, P. D., et al. 2005, ApJ, 625, 796
Hénon, M. 1971a, Ap&SS, 13, 284
Hénon, M. 1971b, Ap&SS, 14, 151
Hoang, B.-M., Naoz, S., Kocsis, B., Rasio, F. A., & Dosopoulou, F. 2018, ApJ,
   856, 140
Hobbs, G., Lorimer, D. R., Lyne, A. G., & Kramer, M. 2005, MNRAS,
   360, 974
Hong, J., Vesperini, E., Askar, A., et al. 2018, MNRAS, 480, 5645
Hurley, J. R., Pols, O. R., & Tout, C. A. 2000, MNRAS, 315, 543
Hurley, J. R., Tout, C. A., & Pols, O. R. 2002, MNRAS, 329, 897
Hut, P. 1981, A&A, 99, 126
Ivanova, N. 2013, MmSAI, 84, 123
Ivanova, N., Chaichenets, S., Fregeau, J., et al. 2010, ApJ, 717, 948
Ivanova, N., Heinke, C. O., Rasio, F. A., Belczynski, K., & Fregeau, J. M.
   2008, MNRAS, 386, 553
Joshi, K. J., Nave, C. P., & Rasio, F. A. 2001, ApJ, 550, 691
Joshi, K. J., Rasio, F. A., Zwart, S. P., & Portegies Zwart, S. 2000, ApJ,
   540, 969
King, I. 1962, AJ, 67, 471
Kiseleva, L. G., Eggleton, P. P., & Mikkola, S. 1998, MNRAS, 300, 292
Kozai, Y. 1962, AJ, 67, 591
Kraus, A. L., Ireland, M. J., Martinache, F., & Hillenbrand, L. A. 2011, ApJ,
  731, 8
Kremer, K., Chatterjee, S., Rodriguez, C. L., & Rasio, F. A. 2018, ApJ, 852, 29
Kremer, K., Chatterjee, S., Ye, C. S., Rodriguez, C. L., & Rasio, F. A. 2019a,
   ApJ, 871, 38
Kremer, K., D'Orazio, D. J., Samsing, J., Chatterjee, S., & Rasio, F. A. 2019b,
   ApJ, 885, 2
Kremer, K., Lu, W., Rodriguez, C. L., Lachat, M., & Rasio, F. 2019c,
  arXiv:1904.06353
Kremer, K., Rodriguez, C. L., Amaro-Seoane, P., et al. 2019d, PhRvD, 99,
Kremer, K., Ye, C. S., Chatterjee, S., Rodriguez, C. L., & Rasio, F. A. 2019e,
   arXiv:1907.12564
Kremer, K., Ye, C. S., Rui, N. Z., et al. 2020, ApJS, 247, 48
Kroupa, P. 2001, MNRAS, 322, 231
Leigh, N. W. C., & Geller, A. M. 2013, MNRAS, 432, 2474
Leigh, N. W. C., Stone, N. C., Geller, A. M., et al. 2016, MNRAS, 463, 3311
Lidov, M. L. 1962, P&SS, 9, 719
Liu, B., Lai, D., & Wang, Y.-H. 2019, ApJ, 881, 41
Liu, B., Muñoz, D. J., & Lai, D. 2015, MNRAS, 447, 747
Lyne, A., Brinklow, A., Middleditch, J., et al. 1987, Natur, 328, 399
```

Mardling, R. A., & Aarseth, S. J. 2001, MNRAS, 321, 398

Mermilliod, J.-C., & Mayor, M. 1999, A&A, 352, 479

Martinez, M. A. S., Fragione, G., Kremer, K., et al. 2020, ApJ, submitted

```
Mermilliod, J.-C., Rosvick, J. M., Duquennoy, A., & Mayor, M. 1992, A&A,
  265, 513
Moody, K., & Sigurdsson, S. 2009, ApJ, 690, 1370
Morscher, M., Pattabiraman, B., Rodriguez, C., Rasio, F. A., & Umbreit, S.
  2015, ApJ, 800, 9
Naoz, S. 2016, ARA&A, 54, 441
Naoz, S., & Fabrycky, D. C. 2014, ApJ, 793, 137
Naoz, S., Farr, W. M., Lithwick, Y., Rasio, F. A., & Teyssandier, J. 2013,
   MNRAS, 431, 2155
Naoz, S., Fragos, T., Geller, A., Stephan, A. P., & Rasio, F. A. 2016, ApJL,
  822, L24
Patience, J., Ghez, A. M., Reid, I. N., Weinberger, A. J., & Matthews, K. 1998,
   AJ, 115, 1972
Pattabiraman, B., Umbreit, S., Liao, W.-K., et al. 2013, ApJS, 204, 15
Perets, H. B., & Fabrycky, D. C. 2009, ApJ, 697, 1048
Perets, H. B., Li, Z., Lombardi, J. C., J., & Milcarek, S. R., J. 2016, ApJ,
  823, 113
Peters, P. 1964, PhRv, 136, B1224
Petrovich, C., & Antonini, F. 2017, ApJ, 846, 146
Prodan, S., & Murray, N. 2012, ApJ, 747, 4
Ransom, S. M. 2008, in IAU Symp. 246, Dynamical Evolution of Dense Stellar
   Systems, ed. E. Vesperini, M. Giersz, & A. Sills (Cambridge: Cambridge
  Univ. Press), 291
Rasio, F. A., McMillan, S., & Hut, P. 1995, ApJL, 438, L33
Riddle, R. L., Tokovinin, A., Mason, B. D., et al. 2015, ApJ, 799, 4
Rivinius, T., Baade, D., Hadrava, P., Heida, M., & Klement, R. 2020, A&A,
Robson, T., Cornish, N. J., & Liu, C. 2019, CQGra, 36, 105011
Rodriguez, C. L., Amaro-Seoane, P., Chatterjee, S., et al. 2018a, PhRvD, 98,
  123005
Rodriguez, C. L., Amaro-Seoane, P., Chatterjee, S., & Rasio, F. A. 2018b,
   PhRvL, 120, 151101
Rodriguez, C. L., Chatterjee, S., & Rasio, F. A. 2016, PhRvD, 93, 084029
Rodriguez, C. L., & Loeb, A. 2018, arXiv:1809.01152
Rodriguez, C. L., Morscher, M., Pattabiraman, B., et al. 2015, PhRvL, 115,
  051101
Rodriguez, C. L., Morscher, M., Wang, L., et al. 2016, MNRAS, 463, 2109
Rose, S. C., Naoz, S., & Geller, A. M. 2019, MNRAS, 488, 2480
Samsing, J., & D'Orazio, D. J. 2018, MNRAS, 481, 5445
Samsing, J., D'Orazio, D. J., Kremer, K., Rodriguez, C. L., & Askar, A. 2019,
  arXiv:1907.11231
Sana, H., Le Bouquin, J.-B., Lacour, S., et al. 2014, ApJS, 215, 15
Sigurdsson, S., & Phinney, E. S. 1993, ApJ, 415, 631
Sigurdsson, S., & Phinney, E. S. 1995, ApJS, 99, 609
Spitzer, L. 1987, Dynamical Evolution of Globular Clusters (Princeton, NJ:
  Princeton Univ. Press)
Stephan, A. P., Naoz, S., Ghez, A. M., et al. 2014, AJ, 147, 87
Stephan, A. P., Naoz, S., Ghez, A. M., et al. 2016, MNRAS, 460, 3494
Stephan, A. P., Naoz, S., Ghez, A. M., et al. 2019, ApJ, 878, 58
Tokovinin, A. 2014, AJ, 147, 86
Toonen, S., Perets, H. B., & Hamers, A. S. 2018, A&A, 610, A22
Valtonen, M., & Karttunen, H. 2006, The Three-Body Problem (Cambridge:
  Cambridge Univ. Press)
Verbunt, F., van Paradijs, J., & Elson, R. 1984, MNRAS, 210, 899
Vink, J. S., de Koter, A., & Lamers, H. J. G. L. M. 2001, A&A, 369, 574
Ye, C. S., Fong, W.-F., Kremer, K., et al. 2020, ApJL, 888, L10
Ye, C. S., Kremer, K., Chatterjee, S., Rodriguez, C. L., & Rasio, F. A. 2019,
       . 877, 122
```

Zevin, M., Samsing, J., Rodriguez, C., Haster, C.-J., & Ramirez-Ruiz, E. 2018,

arXiv:1810.00901